Properties of the Interstellar Medium in Star-Forming Galaxies at $z \sim 1.4$ revealed with ALMA

Akifumi Seko[1], Kouji Ohta[1], Kiyoto Yabe[2,3], Bunyo Hatsukade[2], Masayuki Akiyama[4],
Fumihide Iwamuro[1], Naoyuki Tamura[3], and Gavin Dalton[5,6]

[1]*Department of Astronomy, Kyoto University, Kitashirakawa-Oiwake-Cho, Sakyo-ku, Kyoto, 606-8502, Japan*

seko@kusastro.kyoto-u.ac.jp

[2]*National Astronomical Observatory of Japan, 2-21-1, Osawa, Mitaka, Tokyo, 181-8588, Japan*

[3]*Kavli Institute for the Physics and Mathematics of the Universe, Todai Institutes for Advanced Study, the University of Tokyo, Kashiwa, 277-8583, Japan (Kavli IPMU, WPI)*

[4]*Astronomical Institute, Tohoku University, 6-3 Aramaki, Aoba-ku, Sendai, 980-8578, Japan*

[5]*Department of Astrophysics, University of Oxford, Keble Road, Oxford OX1 3RH, UK*

[6]*STFC RALSpace, Harwell, Oxfordshire OX11 0QX, UK*

ABSTRACT

We conducted observations of ^{12}CO$(J = 5 - 4)$ and dust thermal continuum emission toward twenty star-forming galaxies on the main sequence at $z \sim 1.4$ using ALMA to investigate the properties of the interstellar medium. The sample galaxies are chosen to trace the distributions of star-forming galaxies in diagrams of stellar mass−star formation rate and stellar mass−metallicity. We detected CO emission lines from eleven galaxies. The molecular gas mass is derived by adopting a metallicity-dependent CO-to-H$_2$ conversion factor and assuming a CO(5-4)/CO(1-0) luminosity ratio of 0.23. Molecular gas masses and its fractions (molecular gas mass/(molecular gas mass + stellar mass)) for the detected galaxies are in the ranges of $(3.9 - 12) \times 10^{10}$ $M_\odot$ and $0.25 - 0.94$, respectively; these values are significantly larger than those in local spiral galaxies. The molecular gas mass fraction decreases with increasing stellar mass; the relation holds for four times lower stellar mass than that covered in previous studies, and that the molecular gas mass fraction decreases with increasing metallicity. Stacking analyses also show the same trends. The dust thermal emissions were clearly detected from two galaxies and marginally detected from five galaxies. Dust masses of the detected galaxies are $(3.9 - 38) \times 10^7$ $M_\odot$. We derived gas-to-dust ratios and found they are 3-4 times larger than those in local galaxies. The depletion times of molecular gas for the detected galaxies are $(1.4 - 36) \times 10^8$ yr while the results of the stacking analysis show $\sim 3 \times 10^8$ yr. The depletion time tends to decrease with increasing stellar mass and metallicity though the trend is not so significant, which contrasts with the trends in local galaxies.

Subject headings: galaxies: evolution — galaxies: ISM

1. Introduction

The study of the properties of the interstellar medium (ISM) in galaxies at high redshifts is indispensable for a complete understanding of galaxy evolution. Since galaxies evolve by transforming gas into stars, revealing the amount of gas and its fraction in a galaxy is important to trace galaxy evolution and to understand a stage of the evolution. Since stars eject metals through supernovae explosions and/or mass loss, the dust mass is considered to reflect the star-formation history in a galaxy. In addition, dust plays an important role in formation of hydrogen molecules and in the

cooling of the ISM. Thus, revealing the dust mass and gas-to-dust ratios is also important to understand galaxy evolution.

Most star-forming galaxies form a sequence in the stellar mass−star-formation rate (SFR) diagram at each redshift at least up to $z \sim 2.5$ (e.g., Noeske et al. 2007; Daddi et al. 2007; Rodighiero et al. 2010; Whitaker et al. 2012, 2014), which is called the "main sequence" of star-forming galaxies. It is particularly important to unveil the nature of the ISM in main sequence galaxies at $z = 1 - 2$, because this epoch is the peak of the cosmological evolution of the star-formation rate density (e.g., Hopkins & Beacom 2006; Madau & Dickinson 2014).

Recently, high sensitivity radio telescopes have enabled us to detect CO emission from massive ($M_* > 2.5 \times 10^{10}$ $M_\odot$ assuming a Chabrier initial mass function (IMF: Chabrier 2003)) star-forming galaxies at $z = 1 - 2.5$ (e.g., Daddi et al. 2008, 2010a, 2015; Tacconi et al. 2010, 2013; Genzel et al. 2012, 2013). Tacconi et al. (2010, 2013) derived the molecular gas masses in star-forming galaxies at $z = 1 - 2.5$ ($M_{\rm mol} \sim 10^{10-11}$ $M_\odot$) adopting the Galactic CO-to-H$_2$ conversion factor ($\alpha_{\rm CO} = 4.36$ $M_\odot$ (K km s^{-1} pc^2)$^{-1}$ including helium mass). They found the molecular gas masses to be larger than those in the present-day massive spiral galaxies ($M_{\rm mol} \sim 10^{8.5-10}$ $M_\odot$; e.g., Saintonge et al. 2011a), and that the molecular gas mass fractions [$f_{\rm mol} = M_{\rm mol}/(M_{\rm mol} + M_{\rm star})$] in this stellar mass range are $\sim 30 - 50\%$, after correcting for a bias to larger specific SFR. This range is significantly higher than the typical value in the local massive spiral galaxies ($f_{\rm mol} \sim 8\%$). They also found molecular gas mass fraction tends to decrease with increasing stellar mass.

The recent advent of *Spitzer*/MIPS and *Herschel*/PACS, SPIRE enables us to investigate dust emission in the mid- and far-infrared from high redshift galaxies on the main sequence up to $z \sim 2$ (e.g., Elbaz et al. 2011). Magdis et al. (2012a,b) derived dust masses in main sequence galaxies at $z = 1-3$ ($M_{\rm dust} \sim 10^{8-9}$ $M_\odot$) and showed that the dust mass is larger than that found in present-day spiral galaxies ($M_{\rm dust} \sim 10^{6.5-8}$ $M_\odot$; e.g., Rémy-Ruyer et al. 2014). To investigate the molecular gas content at this redshift, the molecular gas mass was estimated from the dust mass by assuming the gas-to-dust ratio (Magdis et al. 2011, 2012a,b;

Magnelli et al. 2012). These studies also found that galaxies at this redshift show larger molecular gas mass fractions and that the fraction decreases with increasing stellar mass.

Another key parameter that can be used to trace galaxy evolution is the gas-phase metallicity because it reflects past star-forming activity. The relation between stellar mass and metallicity (hereafter mass-metallicity relation) has been studied at $z = 0 - 3$; galaxies with larger stellar mass tend to have higher metallicity (Tremonti et al. 2004; Erb et al. 2006; Maiolino et al. 2008; Moustakas et al. 2011; Zahid et al. 2011, 2013; Yabe et al. 2012, 2014). The mass-metallicity relation seems to be smoothly evolved from $z \sim 3$ to $z \sim 0$; galaxies at higher redshift have systematically lower metallicity at a fixed stellar mass (e.g., Zahid et al. 2013), although the trend may be explained without invoking evolution in terms of the fundamental metallicity relation (e.g., Mannucci et al. 2010; Lara-López et al. 2010). The molecular gas mass fraction is expected to be related to metallicity. At high redshift, however, the relation is unknown, because there are very few CO observations toward the main sequence galaxies with known metallicities. In the local universe, the gas-to-dust ratio also shows a dependence on gas-phase metallicity; the ratio is ~ 150 at solar metallicity and increases with decreasing metallicity (e.g., Leroy et al. 2011; Rémy-Ruyer et al. 2014). In galaxies at $z = 1 - 3$, the ratio is comparable to or a factor of 2 larger than that in nearby galaxies at a fixed metallicity (Saintonge et al. 2013; Seko et al. 2014). However, the number of galaxies with known metallicities at high redshifts that have measurements of both CO and dust remains very limited.

The high sensitivity of the Atacama Large Millimeter/submillimeter Array (ALMA) enables us to study the ISM in star-forming galaxies at high redshift. In this study, we aim to reveal the relations between the molecular gas mass or its fraction and the stellar mass or metallicity for main sequence galaxies at $z \sim 1.4$. In addition, we also examine the dust properties and the gas-to-dust ratio at this redshift. The uniqueness of our sample is that the metallicity has already been measured for each galaxy with near-infrared spectroscopy as described in section 2. Thus, we can also adopt a metallicity-dependent CO-to-H$_2$ con-
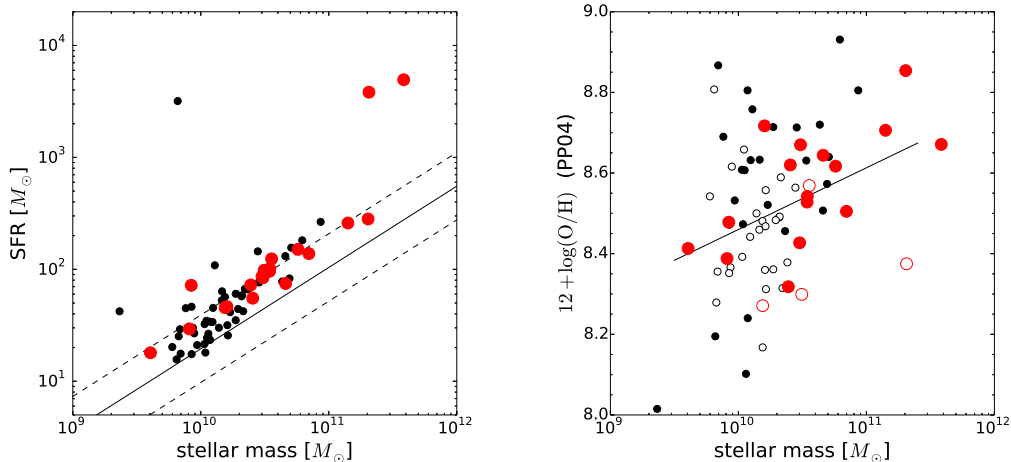
Fig. 1.— (Left) Sample galaxies in the stellar mass-SFR diagram. Circles show 71 Hα emitting galaxies at $z \sim 1.4$ by Yabe et al. (2012) (see text for details). Among them, large (red) circles show 20 sample galaxies observed with ALMA. SFRs are derived from extinction corrected UV luminosity densities. Solid line represents the main sequence at $z \sim 1.4$ by Speagle et al. (2014) after correcting for the difference in IMFs used. Dashed lines show the scatter. (Right) The same sample galaxies in the stellar mass-metallicity diagram. The metallicities are derived from Hα and [NII] emission lines (Pettini & Pagel 2004, PP04 calibration). Large (red) symbols show the ALMA sample galaxies. Objects with [NII] $\lambda6584$ lines with S/N > 1.5 and S/N < 1.5 are indicated by filled and open circles, respectively, i.e., open circles represent upper limits on metallicity. Solid line represents the mass−metallicity relation at $z \sim 1.4$ by Yabe et al. (2014).

version factor. In section 3, the observations and data reduction are described, with source detection for CO emission lines and dust thermal emissions presented in section 4. Results for CO emissions and dust thermal emissions are shown in sections 5 and 6, respectively. Results for gas-to-dust ratio are given in section 7. Throughout this paper, we adopt the standard Λ-CDM cosmology with $H_0 = 70$ km s^{-1} Mpc^{-1}, $\Omega_M = 0.3$, and $\Omega_\Lambda = 0.7$.

2. Samples

Sample galaxies used in this study are taken from Yabe et al. (2012). Yabe et al. (2012) used far-UV and near-UV data taken from Galaxy Evolution Explorer (GALEX) archived image (GR6), U-band images taken from the Canada-France-Hawaii Telescope Legacy Survey (CFHTLS) wide surveys, optical images (B, V, R_C, $i^{'}$, and $z^{'}$-band) from the Subaru-XMM/Newton Deep Sur-

vey (SXDS), the near-infrared images (J, H, and K_s-band) from the DR8 version of the UKIRT Infrared Deep Sky Survey (UKIDSS) Ultra Deep Survey (UDS), and *Spitzer* Infrared Array Camera (IRAC) images (3.6 μm, 4.5 μm, 5.8 μm, and 8.0 μm) from the *Spitzer* public legacy survey of the UKIDSS UDS (SpUDS). Photometric redshift was derived with Hyperz (Bolzonella et al. 2000). Stellar mass was derived by spectral energy distribution (SED) fitting (Sawicki 2012) with the optical to mid-infrared data by employing the population synthesis model by Bruzual & Charlot (2003). SFRs are derived from rest-frame UV luminosity densities, corrected for the dust extinction estimated from the rest-frame UV-slope. In both stellar mass and SFR, the Salpeter IMF (Salpeter 1955) with a mass range of $0.1 - 100$ $M_\odot$ was adopted. Yabe et al. (2012) selected star-forming galaxies at $z \sim 1.4$ with $K_s < 23.9$ mag (AB magnitude) and stellar mass $\geq 10^{9.5}$ $M_\odot$.

Using this sample, Yabe et al. (2012) made

3

near-IR spectroscopic observations with the Fiber Multi-Object Spectrograph (FMOS; Kimura et al. 2010) on the Subaru telescope. Hα emission lines were significantly detected for 71 star-forming galaxies. The stellar mass and SFR for these are shown in Figure 1. The galaxies locate on the main sequence of star-forming galaxies at $z \sim 1.4$ by Speagle et al. (2014). However, the galaxies might be biased to slightly larger SFR, because Yabe et al. (2012) selected galaxies with expected Hα flux larger than 1.0×10^{-16} erg s^{-1} cm^{-2}. The gas metallicities are derived from the N2 method by using the Hα and [NII]λ 6584 emission lines (Pettini & Pagel 2004). It should be noted that Yabe et al. (2015) showed that the nitrogen-to-oxygen abundance ratio in star-forming galaxies at this redshift is significantly higher than the local value at a fixed metallicity and stellar mass, and thus there is a possibility that the metallicity derived with N2 method is systematically overestimated by $0.1 - 0.2$ dex.

We selected 20 of these 71 galaxies as ALMA targets to cover a wide range of stellar mass (4×10^9 - 4×10^{11} $M_\odot$) and metallicity ($12 + \log(\mathrm{O/H}) = 8.2 - 8.9$) and to trace these distributions rather uniformly. The selected sample galaxies are shown with large (red) circles in Figure 1 and listed in Table 1. Almost all of our sample galaxies lie on the main-sequence. The two most massive galaxies (SXDS1_35572 and SXDS1_79307) show very high SFR, and these may not be on the main sequence. The SFR estimation may not be correct for these two galaxies due to, for example, the uncertainty in the dust extinction. Nevertheless, we included these two galaxies to examine their nature. [1] Because the X-ray luminosities ($L_{\mathrm{X}(2-10 \text{ keV})}$) of our sample galaxies are less than 10^{43} erg s^{-1}, they are not X-ray bright active galactic nuclei.

---

[1] It was turned out later that no far-infrared continuum toward these galaxies was detected by *Herschel*, i.e., SFR $\leq$ 50 $M_\odot$ yr^{-1} (Elbaz et al. 2011). SFR of SXDS1_35572 derived from the Hα luminosity is 16 $M_\odot$ yr^{-1} (extinction uncorrected) and 537 $M_\odot$ yr^{-1} (extinction corrected) which is larger than the upper limit from *Herschel* data. Thus, the correction of dust extinction may be overestimated. SFR of SXDS1_79307 from the extinction uncorrected Hα luminosity is 427 $M_\odot$ yr^{-1}. A reason for this large SFR may be that an OH airglow sky emission comes very close to the position of the Hα and we could not completely remove the sky emission.

3. Observations and data reduction

3.1. Observations

We made $^{12}\mathrm{CO}(J = 5 - 4)$ observations toward the 20 galaxies using ALMA. The observations were carried out in 2012 August 9, 11, 15, and 26 during the ALMA cycle0 session (ID=2011.0.00648.S, PI=K. Ohta). The on-source time for each galaxy was $8 - 15$ min. The number of 12 m antennas was 23-25. The observed frequencies were 222.094 GHz to 252.583 GHz (band-6). We used four correlator setups. The frequencies of local oscillator in each setup were 231.198 GHz, 236.168 GHz, 240.380 GHz, and 244.166 GHz. To cover the CO emission lines of all the sample galaxies, we set three or four spectral windows (SPWs) in each correlator setup. Each SPW had a bandwidth of 1.875 GHz. The spectral resolution was 488.28 kHz, corresponding to a velocity resolution of $0.58 - 0.66$ km s^{-1} at the observed frequency range. The FWHM of primary beam was about $26''$. The flux calibration was made with the Ganymede, Uranus, and Callisto. The phase calibrator was J0204 $-$ 170. The bandpass calibrator was J2253 $+$ 161.

3.2. Data reduction

Data reduction was carried out with the Common Astronomy Software Applications (CASA: McMullin et al. 2007) version 4.2 package in a standard manner. The delivered data which were calibrated had problems; the coordinates of the phase calibrator were wrong for three correlator setups (15 target galaxies) and the data of the flux calibrator for a SPW in one correlator setup was flagged for some unknown reason. The coordinates of the phase calibrator were found to be systematically shifted by the $0''.3$ in right ascension and $0''.04$ in declination. Since this shift is not negligible for stacking analysis, we made re-calibrations with the corrected coordinates of the phase calibrator and with the interpolated value for the flagged data of the flux calibrator. We used the 2012 models of the Solar system objects for flux calibrations.

We subtracted the continuum emission in uv-data by using the CASA task UVCONTSUB. Continuum maps were made by combining both the lower side band (LSB) and upper side band (USB)

data in line-free frequencies. The maps were made with the CASA task CLEAN with natural weighting. The center position of each map coincided with the centroid of the galaxy in the K-band image. The number of iteration was zero (i.e., dirty maps) because the signal-to-noise ratios of the detected sources were not high and we were afraid the uncertainty in the maps increases by CLEAN. In addition, since we will discuss the results both for individual galaxy and stacked data below, we employ the same reduction procedure for detected and non-detected galaxies. It should be also noted that no strong sources exist in the fields of view. The synthesized beam size was $0''.6 - 1''.3$ (Table 3). The noise level of continuum map was $0.04 - 0.1$ mJy beam^{-1} (Table 3). For the CO emission studies, we made channel maps from the continuum subtracted data with a velocity resolution of ~ 50 km s^{-1}; the noise level of each channel map was $0.5 - 1$ mJy beam^{-1}.

4. Source detection

The following procedure is employed to search for CO emission lines: The redshifts of our sample galaxies are known from the near-IR spectroscopic observations of Hα emission lines. Thus we derive the "zero velocity" by referring this redshift. We define the "central box", which is the region within $\pm 0''.5$ in right ascension and declination from the map center. Since the angular resolution of our observations is $0''.6 - 1''.3$, the peak position of any CO emission is reasonably expected to be in the central box if signal-to-noise ratio (SN) is ≥ 2.

Using the CASA task IMMOMENTS, we make zeroth-order moment maps (integrated intensity maps) by changing the velocity width ($\Delta v = 50 - 1000$ km s^{-1}) centered at the zero velocity. We measure the SN in the central box for each integrated intensity map and make a SN growth curve against the velocity width. We regard the feature as candidate for detection if the following criteria are satisfied: the highest SN in the growth curve is > 3, the SNs within a velocity width ± 50 km s^{-1} from the velocity width giving the highest SN are also > 3, and the peak positions in the maps lie within the central box.

Since the accuracy of the zero velocity is ~ 150 km s^{-1}, there may be a more appropriate choice of zero velocity. Thus, we change the

"central velocity" of the integrated intensity maps within ± 200 km s^{-1} from the zero velocity and repeat the analysis for all targets.

Among the two analyses mentioned in the above two paragraphs, we take the combination of the central velocity and velocity width which produces the highest-SN peak in the central box. Ten such sources are regarded as candidates for detection.

Next, we make a spectrum of the candidate in the region with SN > 1 around the candidate in the integrated intensity map. If CO emission is also seen adjacent to the velocity width adopted above, we made the integrated intensity map including this velocity range and check whether the map satisfies the criteria mentioned above. Finally, when SN in the spectrum smoothed with the integrated velocity width is > 3, we consider the CO emission to be detected.

In the case of SXDS1_31189, the SNs in the integrated intensity maps for all velocity widths are slightly less than 3, but the emission line is clearly seen in the spectrum at zero velocity. Thus, we consider the CO emission line to be detected. In the case of SXDS2_13316, the SN is ~ 3 at the velocity width of 250 km s^{-1}, but SN is slightly less than 3 when the velocity width changes by ± 50 km s^{-1}. Again, the emission line is very clearly seen in the spectrum. Thus, we also consider this CO emission line to be detected.

In Figure 2, we show the SN growth curves, the integrated intensity maps made with the velocity width shown in the growth curves, and the CO($J = 5 - 4$) line profiles. The peak positions of all the detected source are within $\pm 0''.3$ in right ascension and declination from the map center, confirming that the size of the central box is appropriate.

For the detection of dust thermal emissions, we use the continuum map (right panels of Figure 2). We consider detections for cases where the peak SN in the central box is > 3, and marginal detections if the peak SN is $2 - 3$.

5. Results for CO emission lines

5.1. Individual galaxy

We detected CO($J = 5 - 4$) emission lines from 11 galaxies. These galaxies are shown with filled
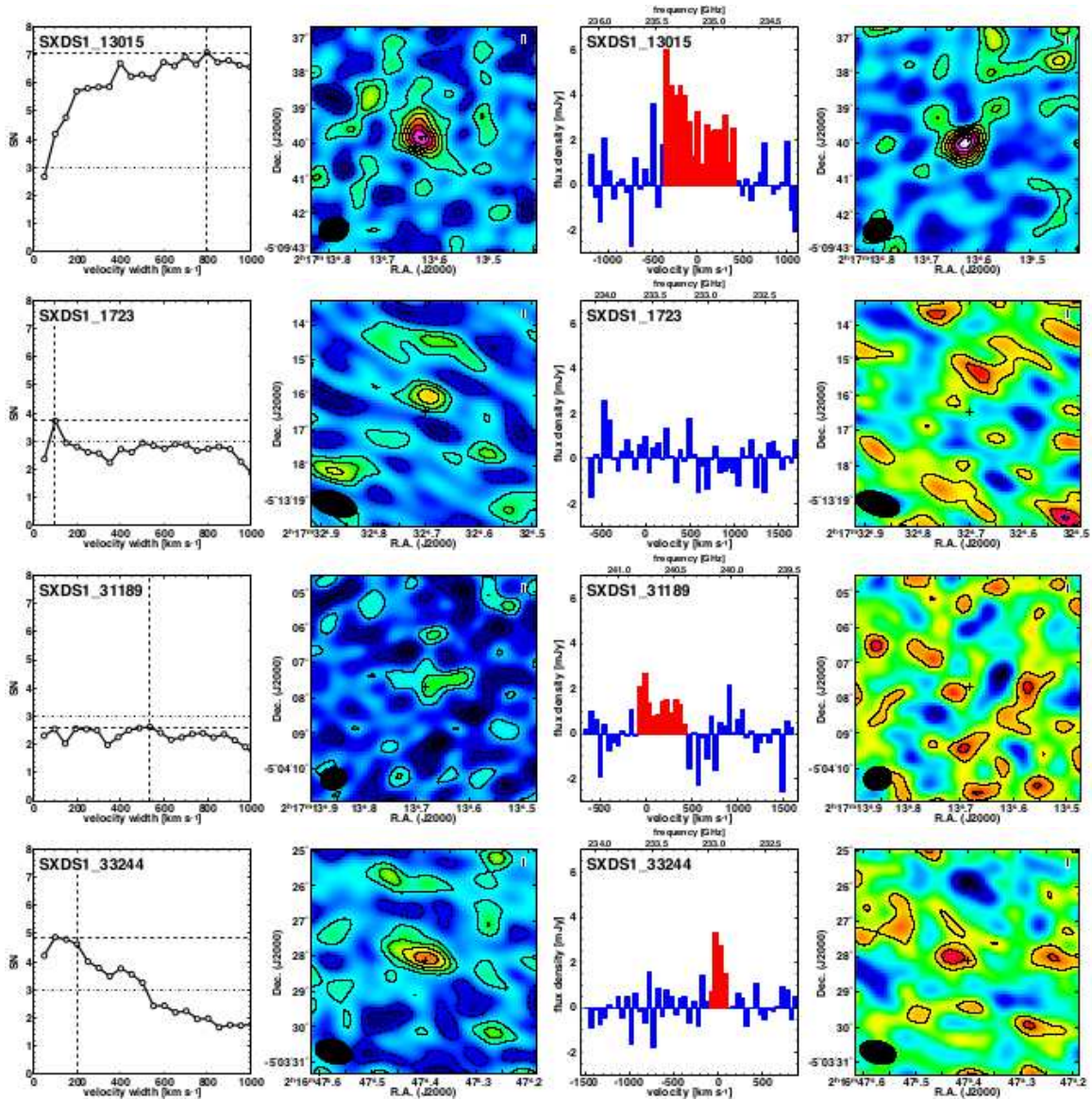
Fig. 2.— (Left) Growth curve of signal-to-noise ratio against integrated velocity width. Horizontal dashed line and dashed-dotted line refer to the peak SN and the SN of 3, respectively. Vertical dashed line refers to the integrated velocity width adopted. (Center Left) Integrated CO(5-4) intensity map. The integrated velocity width is shown with a vertical dashed line in the growth curve of signal-to-noise ratio. Contours represent -2σ, -1σ (dashed lines), 1σ, 2σ, 3σ, ... (solid lines). The cross refers to the peak position in the K-band image. The filled black ellipse at a bottom left corner shows the synthesized beam size. (Center Right) CO(5-4) spectrum. The zero velocity is derived from the spectroscopic redshift of the Hα line. For the CO detected galaxies, the spectra are made in the region where SN is larger than 1 around the source, and the CO emission line is shown with red color. For non-detected galaxies, the spectra are made in the central box. (Right) Continuum map. Contours represent 1σ, 2σ, 3σ, ... (solid lines). The cross refers to the peak position in the K-band image. The filled black ellipse again shows the synthesized beam size.
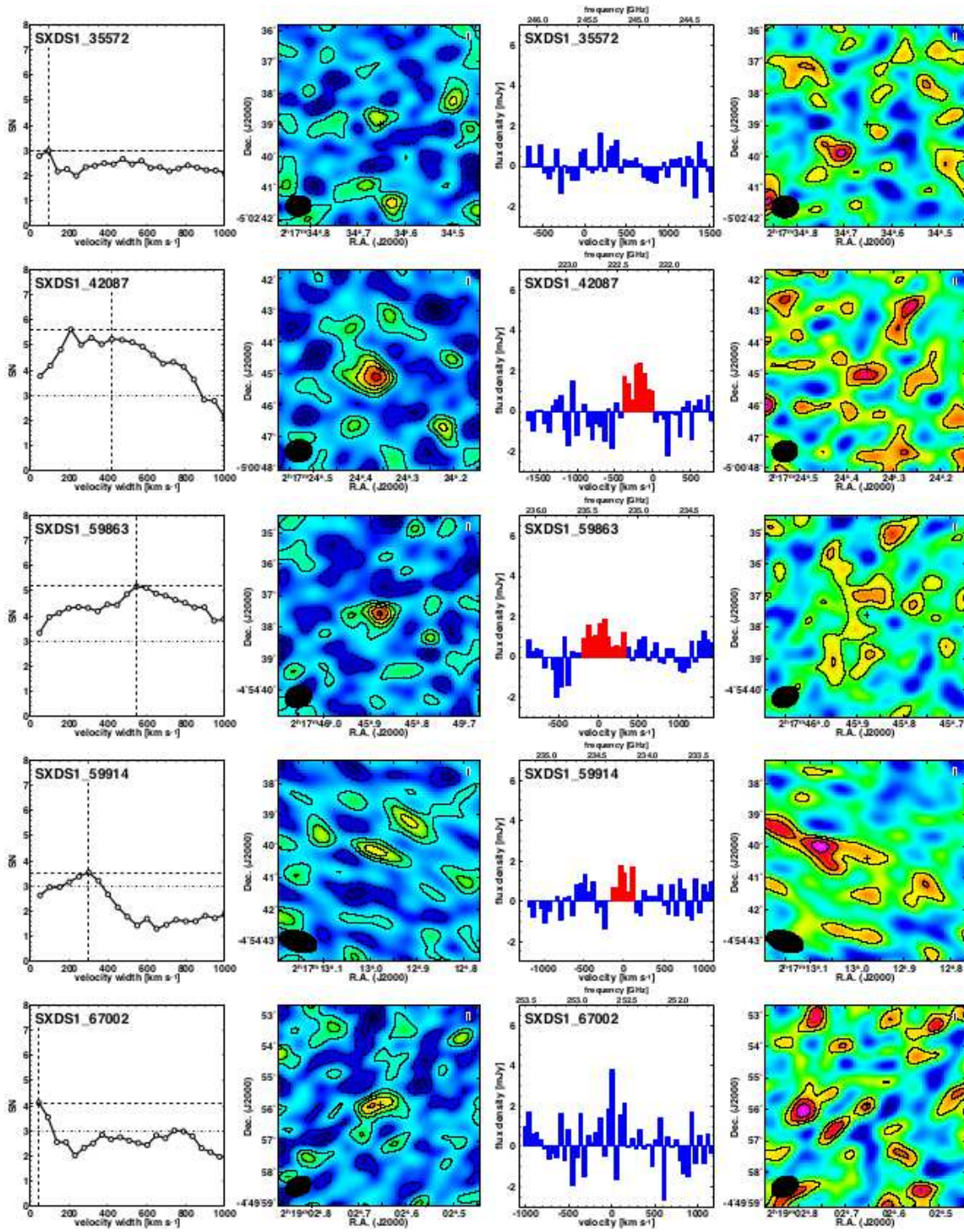
6

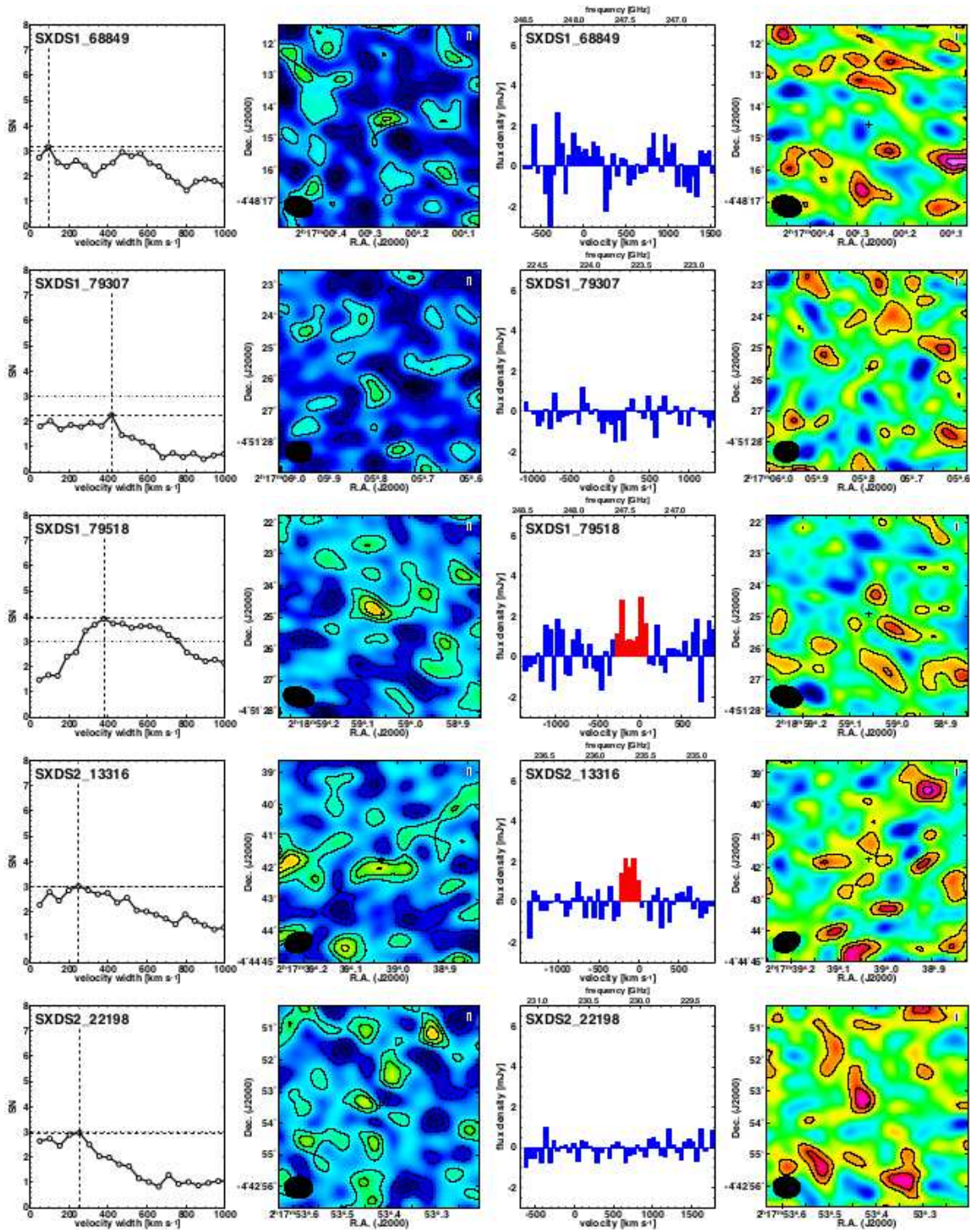Fig. 3.— Same as Figure 2 but for other galaxies.

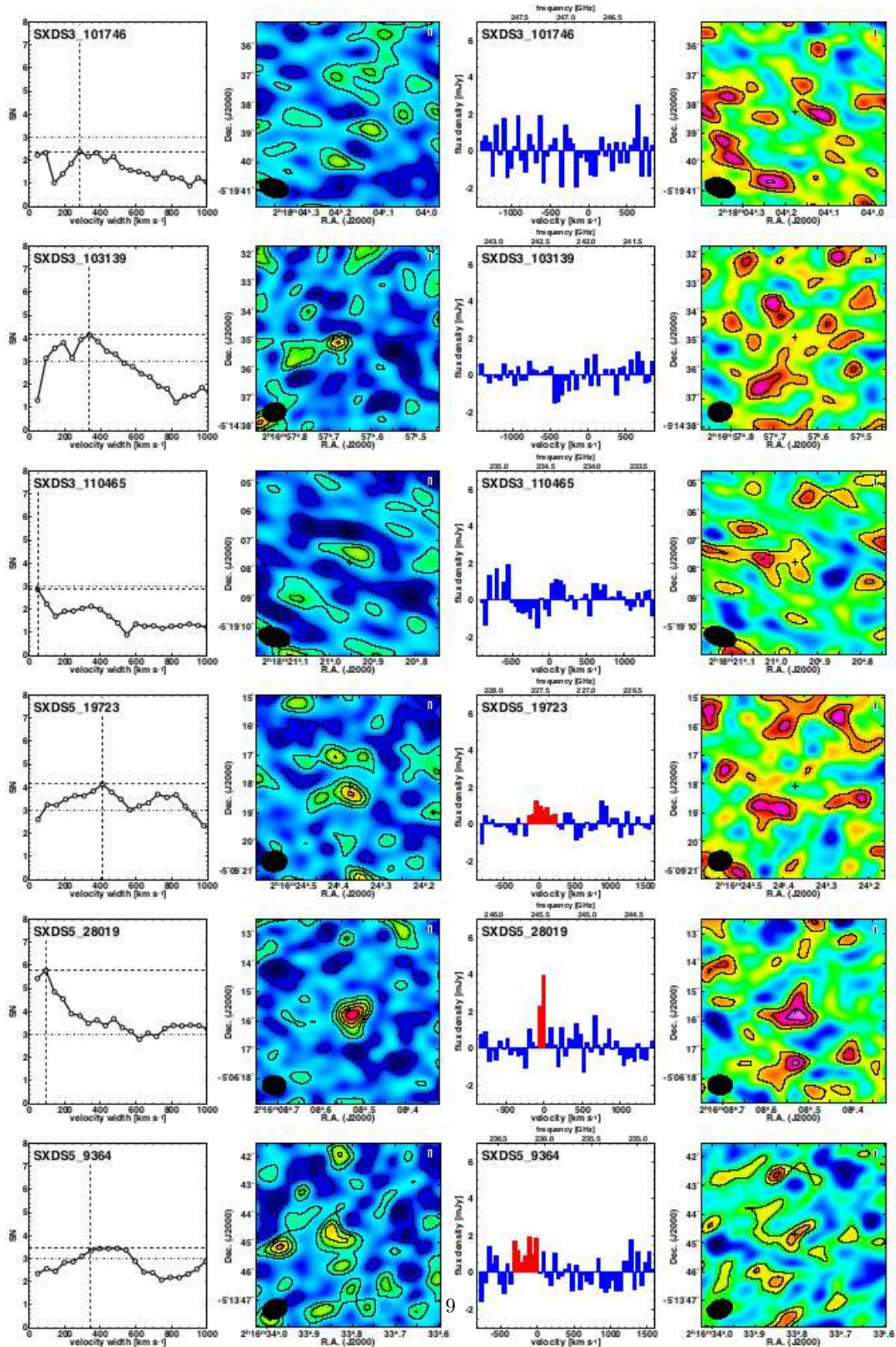Fig. 4.— Same as Figure 2 but for other galaxies. (continued)

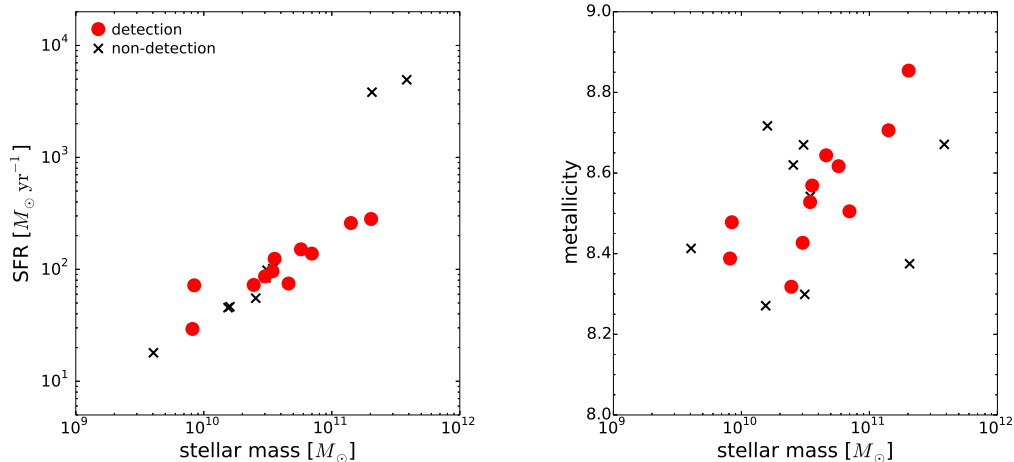Fig. 5.— Same as Figure 2 but for other galaxies. (continued)

Fig. 6.— The location of the observed galaxies in the stellar mass−SFR diagram (Left) and in the stellar mass−metallicity diagram (Right). Filled (red) circles refer to the galaxies for which $CO(J = 5−4)$ emission lines are detected. Crosses show the non-detections.

(red) circles in the stellar mass−SFR and stellar mass−metallicity diagrams (Figure 6). The CO lines tend to be detected for galaxies with more massive/higher SFR on an average. No clear dependence on metallicity is seen, though the average metallicity of the detected galaxies is slightly larger than that of the non-detected galaxies. For the most massive two galaxies (SXDS1_35572 and SXDS1_79307), CO emission lines were not detected, suggesting that the estimation of SFR is not correct for these two galaxies.

The $CO(J = 5 − 4)$ line luminosity $(L'_{CO(5−4)})$ is given as

$$L'_{CO(5−4)} = 3.25 \times 10^7 S_{CO(5−4)} \Delta v \nu_{rest(5−4)}^{-2} D_L^2 (1+z)^{-1},$$
(1)

where $L'_{CO(5−4)}$ is measured in K km s^{-1} pc^2, $S_{CO(5−4)}\Delta v$ is the observed CO(5-4) integrated flux density in Jy km s^{-1}, $\nu_{rest(5−4)}$ is the rest frequency of the CO(5-4) emission line in GHz, and D_L is the luminosity distance in Mpc. For the non-detected galaxies, we make channel maps with a velocity resolution of 200 km s^{-1}, and measure the noise levels (σ_{200}), because the FWHM of the detected CO emission lines range from 45 km s^{-1} to 490 km s^{-1} and the average FWHM is about 200 km s^{-1}. We take a $2\sigma_{200}$ upper limit for the CO(5-4) flux density and a velocity width of

200 km s^{-1}. CO(5-4) luminosities and upper limits are shown in Table 2 and plotted against stellar mass and metallicity in Figure 7. The CO luminosities of the detected galaxies (filled red circles) appear to increase with increasing stellar mass and metallicity.

The molecular gas mass is derived from

$$M_{mol} = \alpha_{CO} L'_{CO(1−0)}.$$
(2)

To derive the molecular gas mass, CO(5-4)/CO(1-0) luminosity ratio is needed. According to a study of the luminosity ratios in three sBzK galaxies at $z \sim 1.5$ (Daddi et al. 2015), the average CO(5-4)/CO(1-0) luminosity ratio is 0.23, corresponding to $S_{CO(5−4)}\Delta v / S_{CO(1−0)}\Delta v \sim 6$, with an uncertainty of a factor of 2. We adopt this value for the conversion of CO(5-4) luminosity to CO(1-0) luminosity. In local galaxies the value of α_{CO} correlates with gas metallicity: the value of α_{CO} is larger in galaxies with lower metallicity (e.g., Arimoto et al. 1996; Leroy et al. 2011). A similar relation is found in star-forming galaxies at $z = 1−2$ (Genzel et al. 2012). We adopt the equation (7) by Genzel et al. (2012):

$$\log(\alpha_{CO}) = -1.3 \times (12 + \log(O/H))_{Denicoló 02} + 12,$$
(3)

where $12 + \log(O/H)_{Denicoló 02}$ is metallicity calibrated by Denicoló et al. (2002). Since we use the
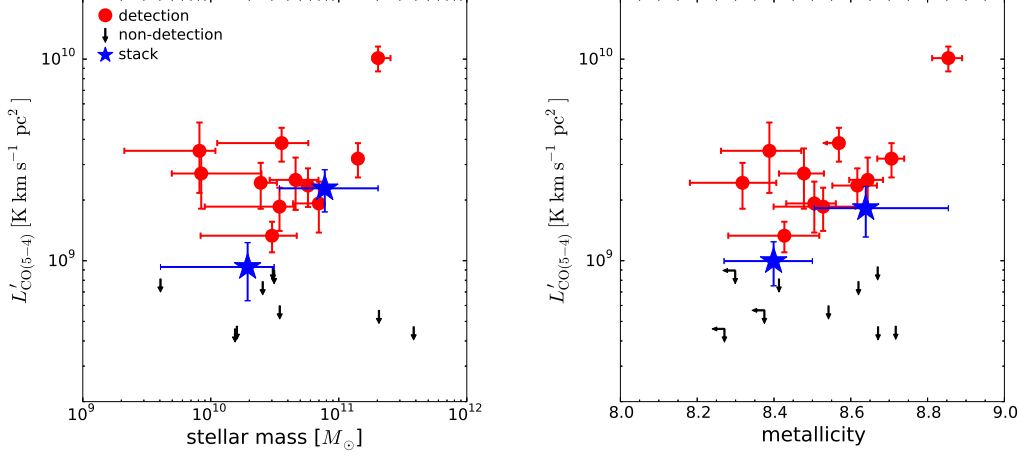
10

Fig. 7.— CO(5-4) luminosity plotted against stellar mass (Left) and metallicity (Right). Filled (red) circles refer to the CO detected galaxies and arrows show the upper limits. Filled (blue) stars refer to the results of stacking analysis for the subsamples with larger/smaller stellar mass in left panel (see the section 5.2.1) and the subsamples with higher/lower metallicity in right panel (see the section 5.2.2).
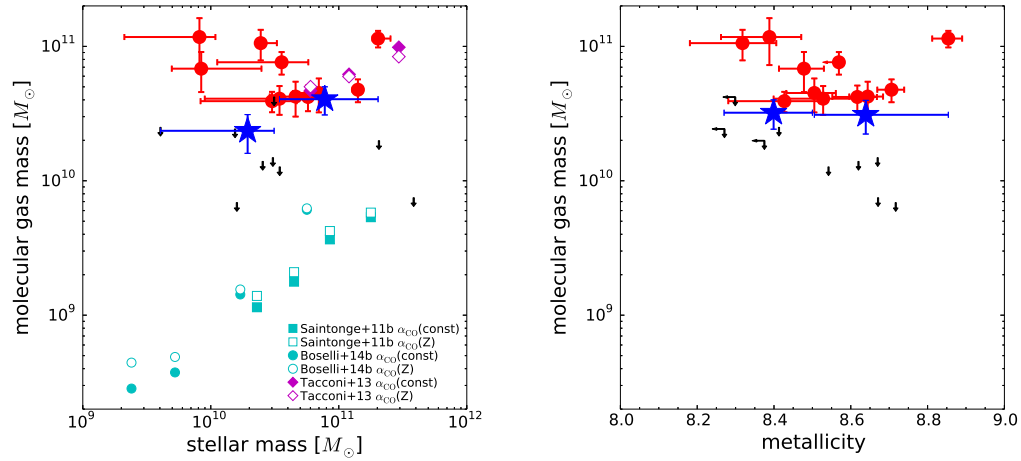

Fig. 8.— Molecular gas mass plotted against stellar mass (Left) and metallicity (Right). We adopted a CO(5-4)/CO(1-0) luminosity ratio of 0.23 and the metallicity-dependent CO-to-H_2 conversion factors shown in the equation 3. Filled (red) circles, arrows, and filled (blue) stars are the same as those in Figure 7. Filled (cyan) squares and circles refer to the average values in local galaxies with a constant CO-to-H_2 conversion factor given by Saintonge et al. (2011a) and Boselli et al. (2014b), respectively. Filled (magenta) diamonds refer to the average values at $z \sim 1.5$ with the Galactic conversion factor (Tacconi et al. 2013). Open (cyan and magenta) symbols show the values obtained with a metallicity-dependent CO-to-H_2 conversion factor. See text for more details.
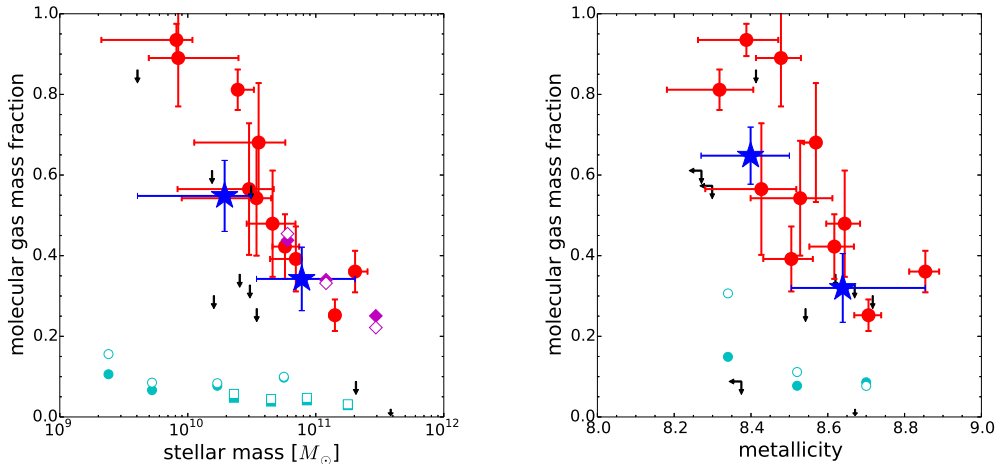
11

Fig. 9.— Molecular gas mass fraction plotted against stellar mass (Left) and metallicity (Right). Symbols are the same as those in Figure 8.

metallicity calibration of Pettini & Pagel (2004), we convert the metallicity using an empirical relation between the two metallicity calibrations of Kewley & Ellison (2008). Derived molecular gas masses are listed in Table 2 and plotted against stellar mass and metallicity in Figure 8. The uncertainty given to the molecular gas mass is based on SN of the integrated intensity map and does not include the uncertainty of the luminosity ratio and $\alpha_{\rm CO}$ (uncertainty of a factor of ~ 2). For the detected galaxies (filled red circles), the molecular gas mass does not seem to depend on stellar mass and metallicity.

The derived molecular gas mass fractions against stellar masses are also listed in Table 2 and plotted against stellar mass and metallicity in Figure 9. For the detected galaxies (filled red circles), the molecular gas mass fraction decreases with increasing stellar mass. This trend is the same in the previous studies (e.g., Tacconi et al. 2013). We show that the trend holds in galaxies with lower stellar mass than have been observed in previous studies. Furthermore, we found that the molecular gas mass fraction decreases with increasing metallicity.

5.2. Stacking analysis

Since the CO emission lines from about half of our sample galaxies are not detected, we car-

ried out a stacking analysis to examine the relations against stellar mass and metallicity. For the stacking analysis, we use images without applying cleaning (i.e., dirty maps). The images are stacked on a pixel by pixel basis using weighted average. The weights are calculated as $1/\sigma^2$, where σ is the R.M.S. noise level in each map. Lindroos et al. (2015) constructed an algorithm for uv-stacking, and they found that image-stacking produced similar results to uv-stacking. To study the properties of the ISM in main sequence galaxies, we did not include the two most massive galaxies, SXDS1_35572 and SXDS1_79307, in our stacking analysis.

For the stacking analysis of CO emission lines, we used channel maps with 50 km s^{-1} bins over a range of ± 1000 km s^{-1} from the zero velocities. Then, we stacked the maps at the same velocity. The detection criteria for the stacked maps are the same as those for the individual galaxies. Error bars of integrated intensity are derived from a random resampling of stacked galaxies. The molecular gas mass is derived using the same CO luminosity ratio and metallicity-dependent CO-to-H$_2$ conversion factor as those used for individual galaxies. The stellar mass and redshift of the stacks are taken to be average values of the stacked galaxies. The metallicity is also derived from stacked FMOS spectra (detailes are described in Yabe et
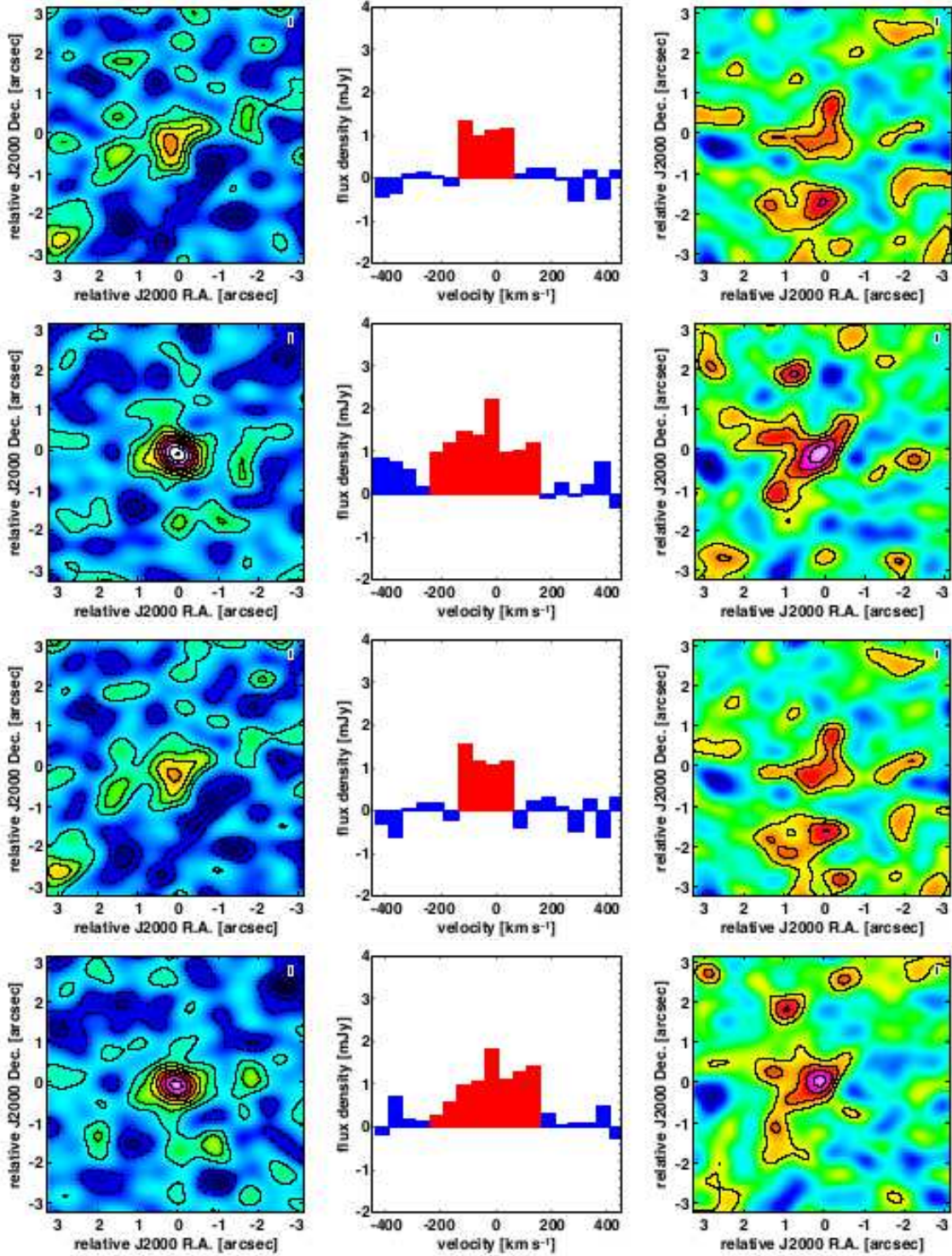
Fig. 10.— (Top left) Stacked integrated CO(5-4) intensity map of the smaller stellar mass subsample (section 5.2.1). Contours represent -2σ, -1σ (dashed lines), 1σ, 2σ, 3σ, ... (solid lines). (Top center) Stacked CO(5-4) spectrum of the smaller stellar mass subsample. CO emission is shown with red color which also shows the velocity range to make the intensity map. The zero velocity is derived by referring the spectroscopic redshift of Hα emission. The spectrum is made in the region where SN is > 1 around the stacked source. (Top right) Stacked continuum map of the smaller stellar mass subsample (section 6.2.1). Contours represent 1σ, 2σ, 3σ, ... (solid lines). (Upper middle) Same as the top row, but for the stacking analysis of the larger stellar mass subsample (section 5.2.1 and 6.2.1). (Lower middle) Same as the top row, but for the stacking analysis of the lower metallicity subsample (section 5.2.2 and 6.2.2). (Bottom) Same as the top row, but for the stacking analysis of the higher metallicity subsample (section 5.2.2 and 6.2.2).

13

al. 2012, 2014).

5.2.1. Stacking analysis of subsamples with larger/smaller stellar mass

In order to examine the dependences of molecular gas mass and gas mass fraction on stellar mass, we carried out a stacking analysis for subsamples with smaller stellar mass ($(0.4 - 3.1) \times 10^{10}$ $M_\odot$, 10 galaxies) and larger stellar mass ($(3.4 - 20) \times 10^{10}$ $M_\odot$, 8 galaxies). The noise levels in the channel maps for these subsamples are similar (~ 0.25 mJy beam^{-1} at a velocity resolution of 50 km s^{-1}). The resulting stacked images for subsamples with smaller and larger stellar mass are shown in left panel of the top and upper middle row of Figure 10, respectively. The stacked profiles are shown in the middle panel of Figure 10. The integrated intensity maps are made with the velocity range shown with red in the profiles. The CO emissions are significantly detected for both subsamples. CO(5 − 4) line luminosities are $(9.3 \pm 3.0) \times 10^8$ K km s^{-1} pc^2 and $(2.3 \pm 0.5) \times 10^9$ K km s^{-1} pc^2 for the smaller and larger stellar mass subsamples, respectively, and are plotted against stellar mass in the left panel of Figure 7 (filled blue stars). We carried out the Welch's t test to evaluate the significance of difference between the stacked values of the subsamples. Here, null hypothesis is that mean values of both subsamples are equal. Significance level for null hypothesis is 0.003%. Thus we regard the CO luminosity significantly increases with increasing stellar mass. The resulting molecular gas masses of the smaller and larger stellar mass subsamples are $(2.4 \pm 0.7) \times 10^{10}$ $M_\odot$ and $(4.0 \pm 1.0) \times 10^{10}$ $M_\odot$, respectively, and are plotted in the left panel of Figure 8 (filled blue stars).

We compare the results with those in local galaxies (CO Legacy Database for Galex Arecibo SDSS Survey (COLD GASS: Saintonge et al. 2011a) and *Herschel* Reference Survey (HRS: Boselli et al. 2014a)). Because the studies in local galaxies used Chabrier IMF, we converted the stellar mass and SFR to those with Salpeter IMF by multiplying 1.7 (Speagle et al. 2014). In addition, the CO-to-H$_2$ conversion factor used in the studies does not include the helium mass and is not corrected for metallicity dependence. Thus, in the left panel of Figure 8, we also plot the local molecular gas mass considering 30% contribution of helium (filled cyan symbols) and the metallicity-dependent CO-to-H$_2$ conversion factor (open cyan symbols: Leroy et al. 2011; Bolatto et al. 2013). We estimated the metallicity of local sample from the mass−metallicity relation in local universe whose metallicity is derived based on N2 method (Erb et al. 2006); Erb et al. (2006) derived the local relation with N2 method by using Sloan Digital Sky Survey (SDSS) galaxies to compare the relation at $z \sim 2$. The study of molecular gas at $z \sim 1.5$ by Tacconi et al. (2013) also used Chabrier IMF and the Galactic CO-to-H$_2$ conversion factor (~ 4.36 $M_\odot$ (K km s^{-1} pc^2)$^{-1}$; including helium mass). We converted the stellar mass and SFR to those with Salpeter IMF and plotted the molecular gas mass in the left panel of Figure 8 (filled magenta diamonds) and plotted that derived with the metallicity-dependent CO-to-H$_2$ conversion factor given by the equation (3) (open magenta diamonds). The metallicity was estimated from the mass−metallicity relation at $z \sim 1.4$ (Yabe et al. 2014). The molecular gas masses of our sample galaxies are significantly larger than those in local star-forming galaxies with similar stellar mass ($M_{\rm mol} \sim 3 \times 10^9$ $M_\odot$; Saintonge et al. 2011a). The molecular gas mass seems to increase with increasing stellar mass (significance level for null hypothesis is 0.25%).

The gas mass fractions are 0.55 ± 0.09 and 0.34 ± 0.08 for the smaller and larger stellar mass subsamples, respectively, and are plotted against stellar mass in the left panel of Figure 9 (filled blue stars). These gas mass fractions are also significantly larger than those in local star-forming galaxies ($f_{\rm mol} \sim 0.08$; Saintonge et al. 2011a). The gas fraction significantly decreases with increasing stellar mass (significance level for null hypothesis is 0.01%). This trend is the same as that in local galaxies (e.g., Saintonge et al. 2011a; Boselli et al. 2014b) and in previous studies at similar redshift (e.g., Tacconi et al. 2013), but our sample extends to the lower stellar mass.

5.2.2. Stacking analysis of subsamples with higher/lower metallicity

In order to examine the dependences of molecular gas mass and gas mass fraction on metallicity, we made stacking analysis for subsamples with lower metallicity ($12 + \log({\rm O/H}) < 8.5$, 7 galaxies) and higher metallicity ($12 + \log({\rm O/H}) > 8.5$,

10 galaxies). We exclude SXDS1_42087 because the metallicity is an upper limit ($12 + \log(\mathrm{O/H}) < 8.57$). The noise levels in the channel maps of these subsamples are similar (~ 0.25 mJy beam^{-1} at a velocity resolution of 50 km s^{-1}). The resulting stacked images for subsamples with lower metallicity and higher metallicity are shown in left panel of the lower middle and bottom rows of Figure 10, respectively. The stacked profiles are shown in the middle panel of Figure 10. The integrated intensity maps are made with the velocity range shown in red in the profiles. The CO emissions are significantly detected for both subsamples. CO$(5 - 4)$ line luminosities are $(1.0 \pm 0.3) \times 10^9$ K km s^{-1} pc^2 and $(1.8 \pm 0.5) \times 10^9$ K km s^{-1} pc^2 for the lower and higher metallicity subsamples, respectively, and are plotted against metallicity in the right panel of Figure 7 (filled blue stars). The CO luminosity seems to increase with increasing metallicity (significance level for null hypothesis is 0.1%). The resulting molecular gas masses of the lower and higher metallicity subsamples are $(3.2 \pm 0.8) \times 10^{10}$ $M_\odot$ and $(3.1 \pm 0.9) \times 10^{10}$ $M_\odot$, respectively, and are plotted in the right panel of Figure 8 (filled blue stars). The molecular gas mass does not depend on metallicity (significance level for null hypothesis is 82%). In this Figure, the result in local star-forming galaxies is not shown. Because Boselli et al. (2014b) showed the molecular gas mass-to-stellar mass ratio but did not show the stellar mass for the metallicity-based analysis, we were not able to calculate the molecular gas mass.

The gas mass fractions are 0.65 ± 0.07 and 0.32 ± 0.09 for the lower and higher metallicity subsamples, respectively, and are plotted against metallicity in the right panel of Figure 9 (filled blue stars). The molecular gas mass fraction significantly decreases with increasing metallicity (significance level for null hypothesis is less than 0.001%).

5.3. Relations for subsamples with fixed metallicity and fixed stellar mass

The relations between gas mass or its fraction and stellar mass or metallicity are examined. Due to the mass-metallicity relation, however, the dependences on stellar mass and metallicity are not clearly separated. Thus we next investigate the dependence only on stellar mass and on metallicity by using a stacking analysis.

First, to avoid the metallicity effect, we made the stacking analysis for subsamples with smaller $((1-4) \times 10^{10}\ M_\odot)$ and larger $((4-15) \times 10^{10}\ M_\odot)$ stellar mass but with almost the same metallicity $(8.50 - 8.75)$. The subsamples with smaller and larger stellar mass include 5 and 4 galaxies, respectively. We exclude SXDS1_42087 because the metallicity is an upper limit of $12 + \log(\mathrm{O/H}) < 8.57$. The average stellar mass and stacked metallicity of the smaller stellar mass subsample are $2.8 \times 10^{10}\ M_\odot$ and 8.61 and those of larger stellar mass subsample are $7.9 \times 10^{10}\ M_\odot$ and 8.63. According to the mass-metallicity relation at $z \sim 1.4$ (e.g., Yabe et al. 2014), the difference of stellar mass in these subsamples $(2.8 \times 10^{10}\ M_\odot$ and $7.9 \times 10^{10}\ M_\odot)$ produces the difference of metallicity of 0.07. Thus, the difference of metallicity in these subsamples (8.61 and 8.63) does not trace the mass-metallicity relation and it is reasonable to consider that only the stellar mass effect can be seen. The resulting molecular gas masses of the smaller and larger stellar mass subsamples are $(1.9 \pm 0.7) \times 10^{10}\ M_\odot$ and $(3.7 \pm 0.6) \times 10^{10}\ M_\odot$, respectively. We plot the result in the upper left panel of Figure 11 (filled blue stars). The trend for the gas mass (significance level for null hypothesis is 0.4%) is the same as that with whole sample galaxies (open stars). The gas mass fractions are 0.40 ± 0.10 and 0.32 ± 0.06 for the smaller and larger stellar mass subsamples, respectively. We plot the result in the upper right panel of Figure 11 (filled blue stars). Although the trend for the gas mass fraction seems to be the same as that for whole sample (open stars), it is not so significant (significance level for null hypothesis is 18%).

Next, to avoid the stellar mass effect, we made the stacking analysis for subsamples with lower (< 8.55) and higher $(8.6 - 8.8)$ metallicity but with comparable stellar mass $(10^{10-11}\ M_\odot)$. The subsamples with lower and higher metallicity both include 5 galaxies. The average stellar mass and stacked metallicity of the lower metallicity subsample are $3.5 \times 10^{10}\ M_\odot$ and 8.41, and those of higher metallicity subsample are $3.5 \times 10^{10}\ M_\odot$ and 8.66. Since there is no difference of stellar mass in these subsamples, it is reasonable to conclude that only the metallicity effect can be seen. The resulting molecular gas masses of the lower and higher

metallicity subsamples are $(5.3 \pm 0.9) \times 10^{10}$ $M_\odot$ and $(2.8 \pm 0.8) \times 10^{10}$ $M_\odot$, respectively. We plot the results in the bottom left panel of Figure 11 (filled blue stars). The molecular gas mass decreases with increasing metallicity (significance level for null hypothesis is 0.2%); this trend is different from that for the whole sample of galaxies (open stars). The gas mass fractions are 0.60 ± 0.07 and 0.45 ± 0.08 for the lower and higher metallicity subsamples, respectively. We also plot the result in the bottom right panel of Figure 11 (filled blue stars). The gas mass fraction seems to decrease with metallicity (significance level for null hypothesis is 1.3%), which is the same trend as seen for the whole sample galaxies (open stars).

6. Results for dust thermal emissions

6.1. Individual galaxy

We detected continuum emission from two galaxies with SN > 3. For five objects, the emissions are marginally detected with $2 < SN < 3$. The positions of these galaxies are in good agreement with the centroid of each galaxy in the K-band image. The detected and marginally detected galaxies are shown with filled circles and open circles, respectively, in the stellar mass−SFR and stellar mass−metallicity diagrams (Figure 12). Continuum emission seems to tend to be detected for more massive galaxies and galaxies with higher metallicity.

The continuum emission is considered to originate from dust thermal emission. The dust mass ($M_{\rm dust}$) is derived as

$$M_{\rm dust} = \frac{S_{\rm cont} D_{\rm L}}{(1+z)\kappa_{\rm d}(\nu_{\rm rest})B(\nu_{\rm rest}, T_{\rm dust})}, \quad (4)$$

where $S_{\rm cont}$ is the observed flux density of dust thermal continuum emission, $\kappa_{\rm d}(\nu_{\rm rest})$ is the dust mass absorption coefficient in the rest-frame frequency ($\sim$ 570 GHz; rest-frame wavelength is $\sim$ 0.5 mm), $T_{\rm dust}$ is the dust temperature, and $B(\nu_{\rm rest}, T_{\rm dust})$ is the Planck function. $\kappa_{\rm d}$ varies with frequency as $\kappa_{\rm d} \propto \nu^\beta$, where β is the dust emissivity index. We adopt $\kappa_{\rm d}(125~\mu m) = 1.875$ m^2 kg^{-1} (Hildebrand 1983), and $\beta = 1.5$. Magnelli et al. (2014) derived dust temperatures of star-forming galaxies in the stellar mass−SFR diagram at $z = 0 - 2.3$. According to their results, the dust temperatures of main sequence galaxies

at $z = 1.2 - 1.7$ are $25 - 35$ K. We adopt a temperature of 30 K. We take a 2σ upper limit as $S_{\rm cont}$, where σ is the R.M.S. noise level in continuum map. The derived dust masses are given in Table 2 and plotted against stellar mass and metallicity in Figure 13. The uncertainty in the dust mass is calculated from the SN of the continuum map. The dust mass can change by a factor of 1.2 when we adopt dust temperatures of 25 or 35 K with a dust emissivity index of 1.5, and change by a factor of 2 when we adopt a dust emissivity indices of 1.0 or 2.0 with a dust temperature of 30 K. No clear dependence on stellar mass or metallicity is seen.

6.2. Stacking analysis

Since the dust thermal continuum emissions from most of the observed galaxies are not detected, we carried out a stacking analysis to examine the dependence on stellar mass and metallicity. For the stacking analysis of dust thermal emission we used uncleaned images. The images are stacked on a pixel by pixel basis using $1/\sigma^2$ weighted average. We do not include SXDS1_35572 and SXDS1_79307 as discussed previously. The detection criteria are the same as those for the individual galaxies. The dust mass is derived with the same dust temperature and dust emissivity index as for the individual galaxies. Error bars are derived from a random resampling of the stacked galaxies.

6.2.1. Stacking analysis of subsamples with larger/smaller stellar mass

To study the stellar mass dependence of dust mass, we carried out a stacking analysis with the subsamples used in section 5.2.1. The stacked continuum maps for the subsamples with smaller and larger stellar mass are shown in the right panel of the top and upper middle rows of Figure 10, respectively. The dust emission is marginally detected for the subsamples with smaller stellar mass, and significantly detected for the subsamples with larger stellar mass. The derived dust masses are $(4.7 \pm 1.6) \times 10^7$ $M_\odot$ and $(1.1 \pm 0.3) \times 10^8$ $M_\odot$ for the subsamples with smaller and larger stellar mass, respectively, and are plotted with blue stars in the left panel of Figure 13. These dust masses are slightly larger than those in local galaxies with the similar stellar mass (Rémy-

Ruyer et al. 2014). The dust masses increase with increasing stellar mass (significance level for null hypothesis is 0.03%).

6.2.2. Stacking analysis of subsamples with higher/lower metallicity

To study the metallicity dependence of dust mass, we carried out a stacking analysis with the subsamples used in section 5.2.2. The stacked continuum maps for the subsamples with lower and higher metallicity are shown in the right panel of the lower middle and bottom rows of Figure 10, respectively. The dust emission is marginally detected for the subsamples with lower metallicity, and significantly detected for the subsamples with higher metallicity. The derived dust masses are $(5.6 \pm 2.2) \times 10^7 \ M_\odot$ and $(7.7 \pm 1.7) \times 10^7 \ M_\odot$ for the subsamples with lower and higher metallicity, respectively, and are plotted with blue stars in the right panel of Figure 13. Although the dust mass seems to increase with increasing metallicity, the trend is not significant (significance level for null hypothesis is 5.8%).

7. Gas-to-dust ratio

Since the molecular gas masses and dust masses have been obtained, we determine gas-to-dust mass ratios in the main sequence galaxies at $z \sim 1.4$, excepting seven galaxies for which only upper limits on both the molecular gas mass and dust mass are obtained. The derived gas-to-dust ratios are shown in Table 2 and plotted in Figure 14. The results of the stacking analyses for the subsamples with lower and higher metallicity are also plotted with blue stars. The gas-to-dust ratios in the subsamples with lower and higher metallicity are 568 ± 261 and 401 ± 142, respectively, and are 3-4 times larger than those in local galaxies at a fixed metallicity (Leroy et al. 2011; Rémy-Ruyer et al. 2014). Moreover, although the gas-to-dust ratios for local galaxies include the HI mass, the ratios at $z \sim 1.4$ do not include this, and so the gas-to-dust ratio in our sample galaxies must be larger than the values derived here. Therefore, care should be taken in deriving molecular gas mass from dust mass by assuming the gas-to-dust ratio in local galaxies.

Seko et al. (2014) observed $CO(J = 2 - 1)$ emission lines from three main sequence galaxies

with solar metallicity at $z \sim 1.4$ detected with Spitzer/MIPS in 24 μm and Herschel/SPIRE in the 250 μm and 350 μm, and derived gas-to-dust ratios. The stacked gas-to-dust ratio of the three galaxies is 250 ± 60 (they assumed $T_{\rm dust} = 35$ K) which is slightly larger than among local galaxies at the same metallicity. However, because the three galaxies observed by Seko et al. (2014) are clearly detected with SPIRE, they may be biased to larger dust masses. On the other hand, because almost all of our sample galaxies in this study are detected neither with MIPS nor SPIRE, there should be little bias to large dust mass.

It is worth mentioning that while we derive the dust mass using a modified black body model with a fixed dust temperature and dust emissivity index, the dust masses in the local galaxies shown in Figure 14 are derived by adopting the models of Draine & Li (2007) (hereafter DL07 models) using Herschel/PACS and SPIRE data. Magdis et al. (2012b) showed that dust masses derived using modified black body models with dust temperatures derived by fitting (average temperature is 33 K) and the same fixed dust emissivity index ($\beta = 1.5$) are about two times smaller than those derived by DL07 models. Hence the gas-to-dust ratios of our samples plotted in Figure 14 would be lower by ~ 0.3 dex, if we used DL07 models. The ratios are still larger by about factor of 2. This result that gas-to-dust ratios in the main sequence galaxies at $z \sim 1.4$ are about two times those for local galaxies is similar to results obtained for lensed galaxies on the main sequence at $z = 1.4 - 3.1$ (Saintonge et al. 2013).

The gas-to-dust ratio at $z \sim 1.4$ seems to decrease with increasing metallicity. Although this trend is the same as that in local galaxies (Leroy et al. 2011; Rémy-Ruyer et al. 2014), since the uncertainty of our results is large, the trend is not significant (significance level for null hypothesis is 16%).

8. Molecular gas mass against SFR, and gas depletion time

We examine the location of our sample galaxies in the molecular gas mass−SFR diagram. In the left panel of Figure 15, the SFRs are derived from extinction corrected UV luminosity densities. In the right panel of Figure 15, the SFRs
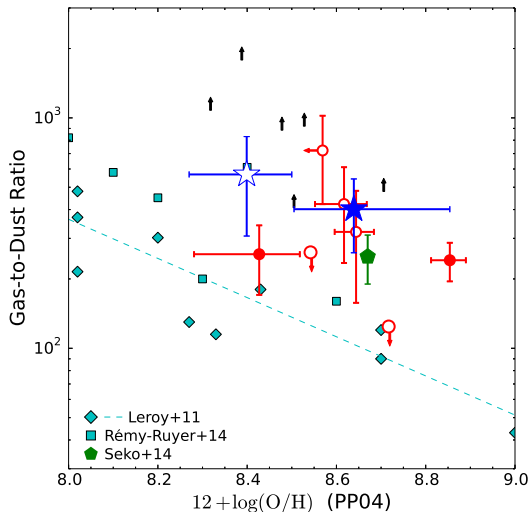
Fig. 14.— Gas-to-dust ratio against metallicity. Filled and open red circles refer to the galaxies from which dust emission is detected significantly and marginally, respectively. Black arrows show the lower limit. Filled/open blue stars refer to the results of stacking analysis for the subsamples with higher/lower metallicity (open symbol refers to marginal detection of dust). Green pentagon refers to the stacked value of three main sequence galaxies at $z \sim 1.4$ by Seko et al. (2014). Cyan diamonds and cyan dashed line represent local galaxies by Leroy et al. (2011), and cyan squares represent the average values in local galaxies shown by Rémy-Ruyer et al. (2014). (Metallicities are calibrated using Pettini & Pagel (2004))

are sum of the SFRs from total infrared luminosities ($L_{IR}(8 - 1000\ \mu\text{m})$; Kennicutt 1998) and the SFRs from extinction uncorrected UV luminosity densities, and are listed in Table 1. L_{IR} are derived by fitting a template SED of main sequence galaxies at $z \sim 1.5$ (Magdis et al. 2012b) to the continuum data obtained in this observation. For the dust detected galaxies, the SFRs from L_{IR} and extinction uncorrected UV luminosity densities roughly agree with those from extinction corrected UV luminosity densities. In this figure, the solid line represents the sequence of normal star-forming galaxies (e.g., local spiral galaxies and sBzK galaxies), and the dashed line rep-

resents the sequence for starburst galaxies (e.g., local ultra luminous infrared galaxies (ULIRGs) and distant submillimeter galaxies (SMGs)) given by Daddi et al. (2010b). Most of CO detected galaxies are located around the solid line.

We carried out a stacking analysis of CO emissions for subsamples with CO detected galaxies ($M_{mol} \geq 3.9 \times 10^{10}\ M_\odot$) and CO non-detected galaxies (almost all of them are $M_{mol} < 2.5 \times 10^{10}\ M_\odot$). We do not include SXDS1_35572 and SXDS1_79307 as discussed previously. The CO emissions are significantly detected for both subsamples. The resulting molecular gas masses of CO detected and non-detected subsamples are $(4.2 \pm 0.6) \times 10^{10}\ M_\odot$ and $(1.1 \pm 0.7) \times 10^{10}\ M_\odot$, respectively. The results of stacking analysis are plotted in the left panel of Figure 15 (filled blue stars). The SFRs derived from extinction corrected UV luminosity densities are taken to be average values of the stacked galaxies. The results of the stacking analysis for the subsamples of CO detected and CO non-detected galaxies are located slightly above the sequence of normal star-forming galaxies and at the middle of the sequences of normal star-forming galaxies and starburst galaxies, respectively.

To derive the SFRs from the L_{IR}, we also carried out a stacking analysis for the same subsamples to see the continuum emission. The dust emission is significantly detected for the subsamples with CO detected, and marginally detected for the subsamples with CO non-detected. The resulting SFRs of CO detected and non-detected subsamples are $(109\pm18)\ M_\odot\ \text{yr}^{-1}$ and $(28\pm14)\ M_\odot\ \text{yr}^{-1}$, respectively. Here, the SFRs derived from extinction uncorrected UV luminosity densities are taken to be average values of the stacked galaxies. The results of stacking analysis are plotted in the right panel of Figure 15 (blue stars), and are located slightly above the sequence of normal star-forming galaxies.

The depletion time of molecular gas is derived by

$$t_{dep} = \frac{M_{mol}}{\text{SFR}}. \qquad (5)$$

The derived depletion times are plotted against stellar mass and metallicity in upper panels of Figure 16. Here, SFRs are derived from extinction corrected UV luminosity densities. For the detected galaxies, the depletion time decreases with

increasing stellar mass and metallicity.

We carried out a stacking analysis for subsamples with smaller and larger stellar mass which were the same subsamples in section 5.2.1. The SFR is taken to be the average of the values of the stacked galaxies. The resulting depletion times are $(3.9 \pm 1.2) \times 10^8$ yr and $(2.6 \pm 0.6) \times 10^8$ yr for the smaller and larger stellar mass subsamples, respectively, and are plotted against stellar mass in upper left panel of Figure 16 (filled blue stars). These values are significantly smaller than those in local star-forming galaxies with similar stellar mass (e.g., Saintonge et al. 2011b; Boselli et al. 2014b). While the depletion time increases with stellar mass in local galaxies, it seems to decrease in the $z \sim 1.4$ star-forming galaxies, though the trend is not so significant (significance level for null hypothesis is 1.0%).

We carried out a stacking analysis for subsamples with lower and higher metallicity which were the same subsamples in section 5.2.2. The resulting depletion times are $(5.3 \pm 1.3) \times 10^8$ yr and $(2.4 \pm 0.7) \times 10^8$ yr for the lower and higher metallicity subsamples, respectively, and are plotted against metallicity in upper right panel of Figure 16 (filled blue stars). The depletion time decreases with increasing metallicity (significance level for null hypothesis is 0.07%), while it seems to increase in local star-forming galaxies.

In lower panels of Figure 16, we also plot depletion times calculated with SFRs from $L_{\rm IR}$ and extinction uncorrected UV luminosity densities. From the stacking analysis, SFRs are (45 ± 12) $M_\odot$ yr^{-1} and (105 ± 21) $M_\odot$ yr^{-1} for the smaller and larger stellar mass subsamples, respectively, and the resulting depletion times are $(5.3 \pm 3.2) \times 10^8$ yr and $(3.9 \pm 1.4) \times 10^8$ yr, respectively (lower left panel of Figure 16 (blue stars)). The depletion time seems to decrease with increasing stellar mass, though the trend is not significant (significance level for null hypothesis is 24%). SFRs are (50 ± 16) $M_\odot$ yr^{-1} and (72 ± 13) $M_\odot$ yr^{-1} for the lower and higher metallicity subsamples, respectively, and the resulting depletion times are $(6.4 \pm 3.6) \times 10^8$ yr and $(4.3 \pm 1.8) \times 10^8$ yr, respectively, (lower right panel of Figure 16 (blue stars)). Although the depletion time seems to decrease with increasing metallicity, the trend is not significant (significance level for null hypothesis is 19%). The similar trend is also seen.

In all cases, the depletion time tends to decrease with increasing stellar mass and metallicity, which contrasts with the trends in local star-forming galaxies; the depletion time increases with increasing stellar mass and metallicity (e.g., Saintonge et al. 2011b; Boselli et al. 2014b). It means that the average star formation efficiency of galaxies with larger stellar mass and metallicity is higher at high redshift, but lower in local universe compared with that of galaxies with smaller stellar mass and metallicity.

9. Summary

To investigate the properties of the interstellar medium in star-forming galaxies at the noon of star-formation rate density, we carried out observations of ^{12}CO$(J = 5 - 4)$ and dust thermal continuum emission toward 20 main sequence galaxies at $z \sim 1.4$ using ALMA. Gas-phase metallicities in these galaxies were derived from near-infrared spectroscopic observations with FMOS on the Subaru telescope using Hα and [NII] emission lines. The range of stellar masses (adopting Salpeter IMF) and metallicities $(12 + \log(\rm O/H))$ of our sample are $4 \times 10^9 - 4 \times 10^{11}$ $M_\odot$ and $8.2 - 8.9$, respectively, and these galaxies uniformly trace the main sequence and mass$-$metallicity relation at this redshift. The stellar mass range covers a lower mass than that reported in previous studies.

We detected CO emission lines from 11 galaxies. The CO lines tend to be detected for galaxies with more massive/higher SFRs. No clear dependence on metallicity is seen, although the average metallicity of the detected galaxies is slightly larger than that of non-detected galaxies. Molecular gas masses are derived by assuming the CO$(5 - 4)$/CO$(1 - 0)$ luminosity ratio of 0.23, and by adopting a metallicity-dependent CO-to-H$_2$ conversion factor. Molecular gas masses and their fraction against stellar mass for the detected galaxies range from $(3.9 - 12) \times 10^{10}$ $M_\odot$ and $0.25 - 0.94$, respectively; these values are significantly larger than those in local spiral galaxies. Since the CO emission lines from about half of our sample galaxies are not detected, we performed stacking analyses to examine the relations of the molecular gas mass and its fraction against stellar mass and metallicity. The results of stacking analyses using the whole sample of galaxies are

that the molecular gas mass is $(2-4) \times 10^{10}\ M_{\odot}$ and increases with increasing stellar mass, but does not depend on metallicity. The molecular gas mass fraction is $30-65\%$ and decreases both with increasing stellar mass and metallicity. Due to the mass−metallicity relation, the dependencies on stellar mass and metallicity are not separated clearly. To avoid the metallicity effect, we performed stacking analyses for subsamples with smaller and larger stellar mass at the almost the same metallicity. The molecular gas mass increases with increasing stellar mass. Its fraction seems to decrease with increasing stellar mass, but the trend is not so significant. To avoid the stellar mass effect, we made stacking analyses for subsamples with lower and higher metallicity at the almost same stellar mass. Both the molecular gas mass and its fraction decrease with increasing metallicity.

We detected significant continuum emissions from 2 galaxies with marginal detections from a further 5 galaxies. Continuum emissions tend to be detected for galaxies with larger stellar mass and with higher metallicity. Dust masses were derived with a modified black body model by adopting a dust temperature of 30 K and a dust emissivity index of 1.5. The derived dust masses of the detected galaxies are $(3.9-38) \times 10^{7}\ M_{\odot}$. We used stacking analyses to examine the relations of the dust mass against stellar mass and metallicity. The dust mass increases with increasing stellar mass and seems to increase with increasing metallicity.

We also derive the gas-to-dust ratio. The result of stacking the subsamples with lower and higher metallicity shows that the gas-to-dust ratios are ~ 500, which is 3-4 times larger than those in local galaxies at the same metallicity range. The gas-to-dust ratio at $z \sim 1.4$ seems to decrease with increasing metallicity.

CO detected galaxies locate around the sequence of normal star-forming galaxies in the molecular gas mass−SFR diagram. The results of stacking analysis show that the depletion time of molecular gas is $\sim 3 \times 10^{8}$ yr which is smaller than that in local galaxies. Although the uncertainty of depletion time is large, the timescale tends to decrease with increasing stellar mass and metallicity. These trends contrast with those in local star-forming galaxies.

REFERENCES

Arimoto, N., Sofue, Y., & Tsujimoto, T. 1996, PASJ, 48, 275

Bolatto, A. D., Wolfire, M., & Leroy, A. K. 2013, ARA&A, 51, 207

Bolzonella, M., Miralles, J.-M., & Pelló, R. 2000, A&A, 363, 476

Boselli, A., Cortese, L., & Boquien, M. 2014, A&A, 564, A65

Boselli, A., Cortese, L., Boquien, M., et al. 2014, A&A, 564, A66

Bruzual, G., & Charlot, S. 2003, MNRAS, 344, 1000

Chabrier, G. 2003, PASP, 115, 763

Daddi, E., Bournaud, F., Walter, F., et al. 2010a, ApJ, 713, 686

Daddi, E., Dannerbauer, H., Elbaz, D., et al. 2008, ApJ, 673, L21

Daddi, E., Dannerbauer, H., Liu, D., et al. 2015, A&A, 577, A46

Daddi, E., Dickinson, M., Morrison, G., et al. 2007, ApJ, 670, 156

Daddi, E., Elbaz, D., Walter, F., et al. 2010b, ApJ, 714, L118

Denicoló, G., Terlevich, R., & Terlevich, E. 2002, MNRAS, 330, 69

Draine, B. T., & Li, A. 2007, ApJ, 657, 810

Elbaz, D., Dickinson, M., Hwang, H. S., et al. 2011, A&A, 533, A119

Erb, D. K., Shapley, A. E., Pettini, M., et al. 2006, ApJ, 644, 813

Genzel, R., Tacconi, L. J., Combes, F., et al. 2012, ApJ, 746, 69

Genzel, R., Tacconi, L. J., Kurk, J., et al. 2013, ApJ, 773, 68

Hildebrand, R. H. 1983, QJRAS, 24, 267

Hopkins, A. M., & Beacom, J. F. 2006, ApJ, 651, 142

Kennicutt, R. C., Jr. 1998, ARA&A, 36, 189

Kewley, L. J., & Ellison, S. L. 2008, ApJ, 681, 1183

Kimura, M., Maihara, T., Iwamuro, F., et al. 2010, PASJ, 62, 1135

Lara-López, M. A., Cepa, J., Bongiovanni, A., et al. 2010, A&A, 521, L53

Leroy, A. K., Bolatto, A., Gordon, K., et al. 2011, ApJ, 737, 12

Lindroos, L., Knudsen, K. K., Vlemmings, W., Conway, J., & Martí-Vidal, I. 2015, MNRAS, 446, 3502

Madau, P., & Dickinson, M. 2014, ARA&A, 52, 415

Magdis, G. E., Daddi, E., Béthermin, M., et al. 2012b, ApJ, 760, 6

Magdis, G. E., Daddi, E., Elbaz, D., et al. 2011, ApJ, 740, L15

Magdis, G. E., Daddi, E., Sargent, M., et al. 2012a, ApJ, 758, L9

Magnelli, B., Lutz, D., Saintonge, A., et al. 2014, A&A, 561, AA86

Magnelli, B., Saintonge, A., Lutz, D., et al. 2012, A&A, 548, A22

Maiolino, R., Nagao, T., Grazian, A., et al. 2008, A&A, 488, 463

Mannucci, F., Cresci, G., Maiolino, R., Marconi, A., & Gnerucci, A. 2010, MNRAS, 408, 2115

McMullin, J. P., Waters, B., Schiebel, D., Young, W., & Golap, K. 2007, Astronomical Data Analysis Software and Systems XVI, 376, 127

Moustakas, J., Zaritsky, D., Brown, M., et al. 2011, arXiv:1112.3300

Noeske, K. G., Weiner, B. J., Faber, S. M., et al. 2007, ApJ, 660, L43

Pettini, M., & Pagel, B. E. J. 2004, MNRAS, 348, L59

Rémy-Ruyer, A., Madden, S. C., Galliano, F., et al. 2014, A&A, 563, A31

Rodighiero, G., Cimatti, A., Gruppioni, C., et al. 2010, A&A, 518, L25

Saintonge, A., Kauffmann, G., Kramer, C., et al. 2011a, MNRAS, 415, 32

Saintonge, A., Kauffmann, G., Wang, J., et al. 2011b, MNRAS, 415, 61

Saintonge, A., Lutz, D., Genzel, R., et al. 2013, ApJ, 778, 2

Salpeter, E. E. 1955, ApJ, 121, 161

Sawicki, M. 2012, PASP, 124, 1208

Seko, A., Ohta, K., Hatsukade, B., et al. 2014, PASJ, 66, 81

Speagle, J. S., Steinhardt, C. L., Capak, P. L., & Silverman, J. D. 2014, ApJS, 214, 15

Tacconi, L. J., Genzel, R., Neri, R., et al. 2010, Nature, 463, 781

Tacconi, L. J., Neri, R., Genzel, R., et al. 2013, ApJ, 768, 74

Tremonti, C. A., Heckman, T. M., Kauffmann, G., et al. 2004, ApJ, 613, 898

Whitaker, K. E., van Dokkum, P. G., Brammer, G., & Franx, M. 2012, ApJ, 754, L29

Whitaker, K. E., Franx, M., Leja, J., et al. 2014, ApJ, 795, 104

Yabe, K., Ohta, K., Akiyama, M., et al. 2015, PASJ, in press (arXiv:1508.01512)

Yabe, K., Ohta, K., Iwamuro, F., et al. 2012, PASJ, 64, 60

Yabe, K., Ohta, K., Iwamuro, F., et al. 2014, MNRAS, 437, 3647

Zahid, H. J., Geller, M. J., Kewley, L. J., et al. 2013, ApJ, 771, L19

Zahid, H. J., Kewley, L. J., & Bresolin, F. 2011, ApJ, 730, 137
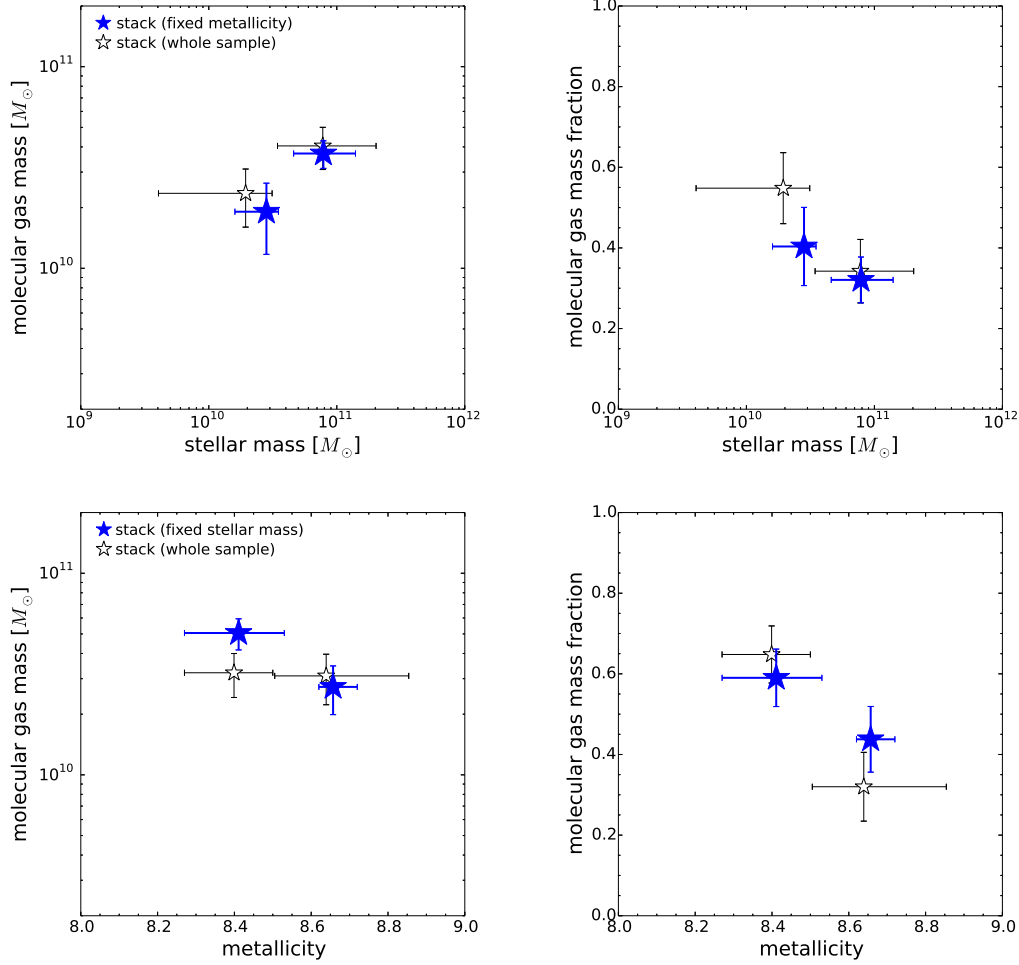
Fig. 11.— Molecular gas mass (upper left) and molecular gas mass fraction (upper right) against stellar mass. Large filled blue stars refer to the stacking analysis for the subsamples with larger/smaller stellar mass but with almost the same stacked metallicity. Small open stars refer to the stacking analysis for the subsamples with larger/smaller stellar mass using the whole sample. Molecular gas mass (bottom left) and molecular gas mass fraction (bottom right) against metallicity. Large filled blue stars refer to the stacking analysis for the subsamples with higher/lower metallicity but with the same average stellar mass. Small open stars refer to the stacking analysis for the subsamples with higher/lower metallicity using the whole sample.
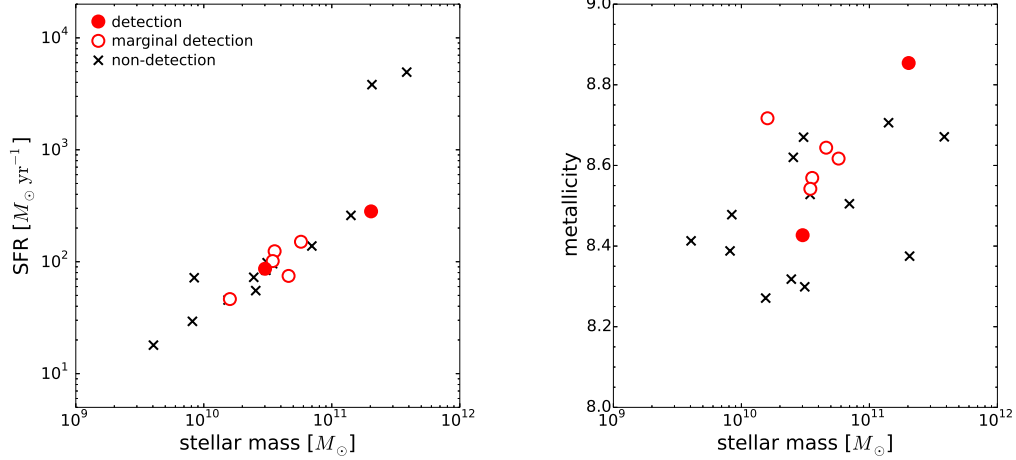
Fig. 12.— Observed galaxies in the stellar mass−SFR diagram (Left) and in the stellar mass−metallicity diagram (Right). Filled and open (red) circles refer to the galaxies for which the continuum emissions are significantly and marginally detected, respectively. The crosses show non-detections.
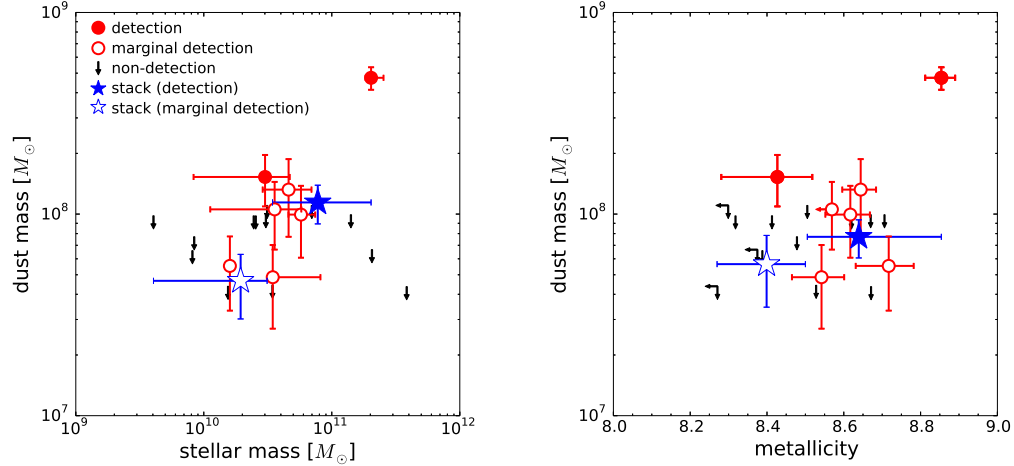
Fig. 13.— Dust mass against stellar mass (Left) and against metallicity (Right). Dust masses are derived using a modified black body model by assuming a dust temperature of 30 K and a dust emissivity index of 1.5. The filled and open (red) circles refer to the galaxies for which the continuum emissions are significantly and marginally detected, respectively. Arrows show the upper limits. Filled/open (blue) stars refer to the results of the stacking analyses for the subsamples with larger/smaller stellar mass in left panel (see the section 6.2.1) and the subsamples with higher/lower metallicity in right panel (see the section 6.2.2).
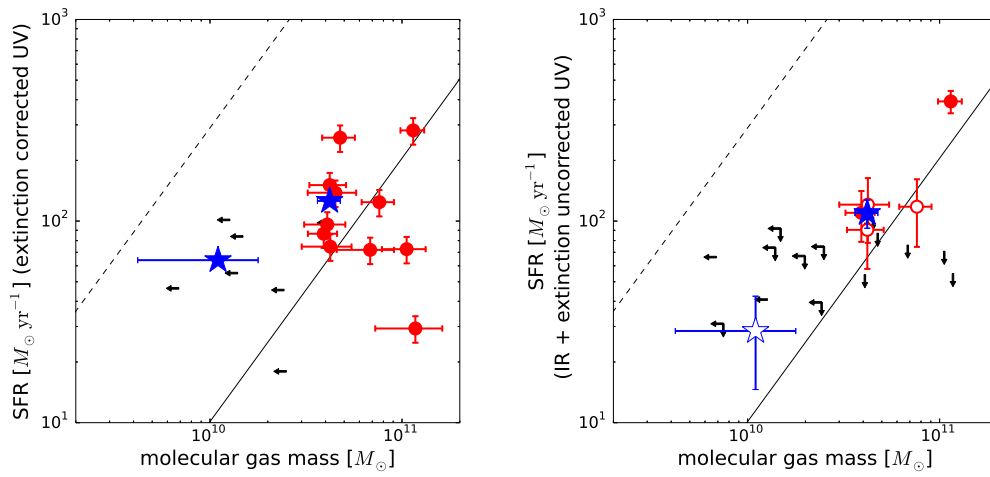
Fig. 15.— SFR against molecular gas mass. (Left) SFRs are derived from extinction corrected UV luminosity densities. Filled (red) circles refer to the CO detected galaxies and (black) left arrows show the CO non-detected galaxies. Filled (blue) stars refer to the results of stacking analysis for the subsamples of CO detected and non-detected. (Right) SFRs are sum of the SFRs from total infrared luminosities and the SFRs from extinction uncorrected UV luminosity densities. Filled (red) circles refer to the both CO and dust detected galaxies. Down-arrows show the dust non-detected galaxies but CO emissions are detected. Stars and left arrows are the same as those in the left panel. Open symbols represent the marginal detections of dust continuum emission. Solid and dashed lines represent the sequences of normal star-forming galaxies (e.g., local spirals and sBzK galaxies) and starburst galaxies (e.g., local ULIRGs and SMGs), respectively, given by Daddi et al. (2010b).
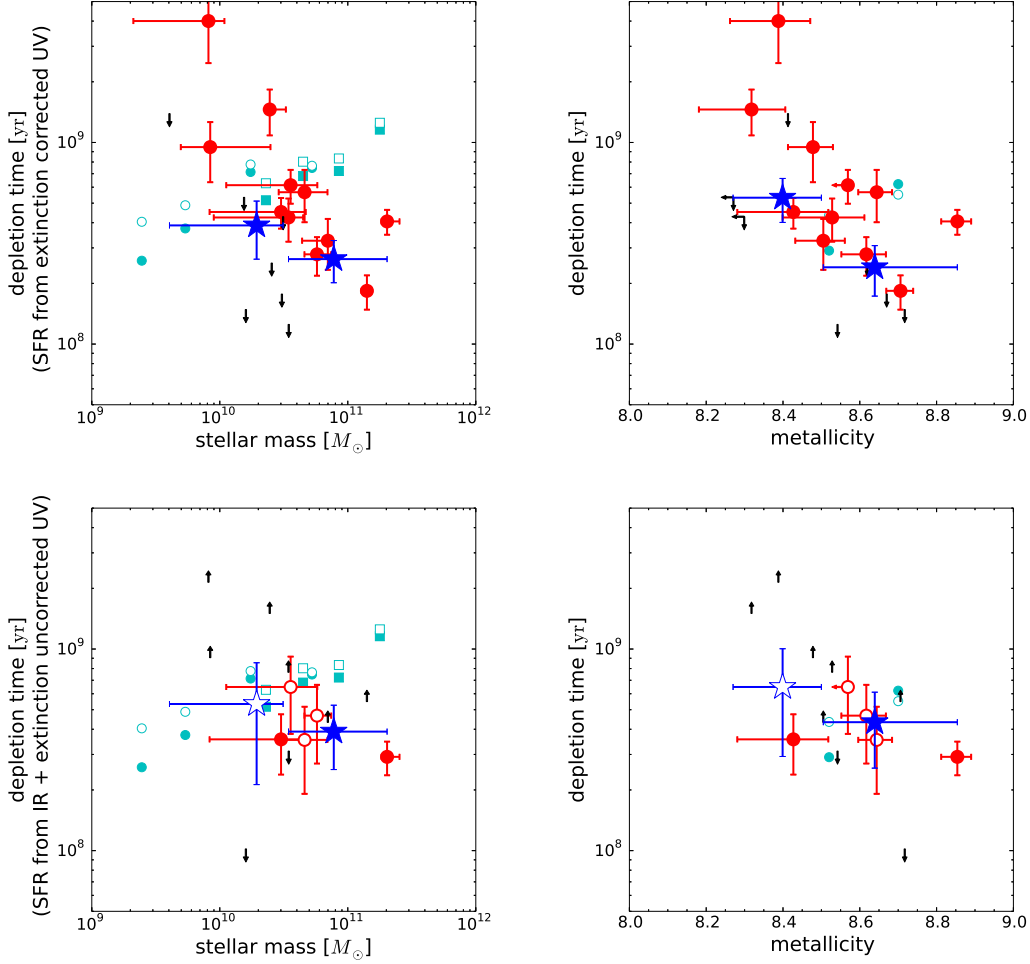
Fig. 16.— Depletion time of molecular gas calculated with SFR from extinction corrected UV luminosity density against stellar mass (upper left) and against metallicity (upper right). Symbols are the same as those in Figure 8. Depletion time of molecular gas calculated with SFR from total infrared luminosity and extinction uncorrected UV luminosity density against stellar mass (lower left) and against metallicity (lower right). Filled (red) circles refer to the both CO and dust detected galaxies. Open (red) circles refer to the CO detected and dust marginally detected galaxies. Filled/open blue stars refer to the results of stacking analysis (open symbol refers to galaxies with marginally detected dust emission). Arrows show the upper and lower limits.

26

Table 1

Table 1

Sample galaxies.

ID	RA[a] (J2000)	DEC[a] (J2000)	$z_{\rm spec}$[b]	M_*[c] ($M_\odot$)	metallicity[d] $12 + \log{(O/H)}$	SFR[c] ($M_\odot$ yr^{-1})	SFR[e] ($M_\odot$ yr^{-1})	SFR[f] ($M_\odot$ yr^{-1})
SXDS1_13015	02:17:13.63	-05:09:39.8	1.451	$(2.0^{+0.5}_{-0.2}) \times 10^{11}$	$8.85^{+0.04}_{-0.04}$	282	154	392 ± 50
SXDS1_1723	02:17:32.70	-05:13:16.5	1.467	$(3.1^{+3.0}_{-2.0}) \times 10^{10}$	< 8.30	98	154	< 107
SXDS1_31189	02:17:13.68	-05:04:07.7	1.394	$(8.2^{+2.7}_{-6.0}) \times 10^{9}$	$8.39^{+0.08}_{-0.13}$	29	72	< 55
SXDS1_33244	02:16:47.40	-05:03:28.1	1.474	$(5.7^{+1.7}_{-1.2}) \times 10^{10}$	$8.62^{+0.05}_{-0.07}$	151	189	90 ± 33
SXDS1_35572	02:17:34.65	-05:02:39.0	1.347	$(3.8^{+0.1}_{-1.1}) \times 10^{11}$	$8.67^{+0.08}_{-0.09}$	4938	537	< 31
SXDS1_42087	02:17:24.36	-05:00:44.9	1.594	$(3.6^{+2.2}_{-2.5}) \times 10^{10}$	< 8.57	124	143	118 ± 43
SXDS1_59863	02:17:45.88	-04:54:37.6	1.448	$(1.4^{+0.1}_{-0.1}) \times 10^{11}$	$8.71^{+0.03}_{-0.04}$	259	228	< 87
SXDS1_59914	02:17:12.98	-04:54:40.4	1.460	$(7.0^{+0.0}_{-2.6}) \times 10^{10}$	$8.51^{+0.06}_{-0.07}$	138	188	< 105
SXDS1_67002	02:19:02.65	-04:49:55.9	1.281	$(3.5^{+4.7}_{-0.1}) \times 10^{10}$	$8.54^{+0.06}_{-0.08}$	101	88	41 ± 13
SXDS1_68849	02:17:00.28	-04:48:14.5	1.325	$(2.5^{+2.1}_{-1.9}) \times 10^{10}$	$8.62^{+0.04}_{-0.05}$	55	70	< 74
SXDS1_79307	02:17:05.79	-04:51:25.7	1.575	$(2.1^{+0.0}_{-0.0}) \times 10^{11}$	< 8.38	3822	10474	< 67
SXDS1_79518	02:18:59.06	-04:51:24.9	1.330	$(2.5^{+0.8}_{-0.2}) \times 10^{10}$	$8.32^{+0.09}_{-0.14}$	73	146	< 71
SXDS2_13316	02:17:39.03	-04:44:41.8	1.446	$(8.4^{+16}_{-3.5}) \times 10^{9}$	$8.48^{+0.05}_{-0.07}$	72	118	< 76
SXDS2_22198	02:17:53.42	-04:42:53.4	1.499	$(1.6^{+0.1}_{-0.1}) \times 10^{10}$	$8.72^{+0.07}_{-0.09}$	46	87	66 ± 17
SXDS3_101746	02:18:04.18	-05:19:38.3	1.335	$(4.0^{+1.3}_{-0.8}) \times 10^{9}$	$8.41^{+0.07}_{-0.09}$	18	70	< 75
SXDS3_103139	02:16:57.65	-05:14:34.9	1.382	$(1.5^{+0.7}_{-0.1}) \times 10^{10}$	< 8.27	45	68	< 39
SXDS3_110465	02:18:20.95	-05:19:07.7	1.458	$(3.1^{+2.3}_{-0.8}) \times 10^{10}$	$8.67^{+0.03}_{-0.03}$	84	90	< 92
SXDS5_19723	02:16:24.37	-05:09:18.1	1.533	$(3.4^{+1.0}_{-2.5}) \times 10^{10}$	$8.53^{+0.08}_{-0.13}$	96	162	< 54
SXDS5_28019	02:16:08.53	-05:06:15.6	1.348	$(3.0^{+1.7}_{-2.2}) \times 10^{10}$	$8.43^{+0.09}_{-0.15}$	87	104	110 ± 31
SXDS5_9364	02:16:33.81	-05:13:44.7	1.441	$(4.6^{+2.3}_{-1.7}) \times 10^{10}$	$8.64^{+0.04}_{-0.05}$	75	102	121 ± 43

[a]The accuracy of coordinates in the K-band image is $\sim 0''.2 - 0''.3$.

[b]Derived from Hα wavelength in vacuum. The error is typically ± 0.001.

[c]We adopted Salpeter IMF (Salpeter 1955). SFR is derived from extinction corrected UV luminosity density. The error of SFR is typically 15%.

[d]Derived from Hα and [NII]λ 6584 calibrated by Pettini & Pagel (2004).

[e]SFR is derived from extinction corrected Hα luminosity density. The error of SFR is typically 10%.

[f]Sum of SFR from $L_{\rm IR}(8 - 1000~\mu{\rm m})$ from our dust continuum observations and SFR from extinction uncorrected UV luminosity densities.

Table 2

Results of the observations.

ID	$\int S_{CO(5-4)}dv$ (Jy km s^{-1})	$L'_{CO(5-4)}$ (10^9 K km s^{-1} pc^2)	M_{gas}[a] (10^{10} $M_\odot$)	f_{gas}[b]	$S_{continuum}$[c] (mJy)	M_{dust}[d] (10^7 $M_\odot$)	Gas-to-Dust Ratio
SXDS1_13015	2.31 ± 0.33	10 ± 1	11 ± 2	0.36 ± 0.05	0.86 ± 0.11	47 ± 6	241 ± 46
SXDS1_1723	< 0.20	< 0.9	< 4.2	< 0.57	< 0.20	< 11	──
SXDS1_31189	0.86 ± 0.33	3.5 ± 1.3	12 ± 4	0.94 ± 0.04	< 0.12	< 6.6	> 1783
SXDS1_33244	0.52 ± 0.11	2.4 ± 0.5	4.2 ± 0.9	0.42 ± 0.08	0.18 ± 0.07	9.9 ± 3.9	423 ± 188
SXDS1_35572	< 0.12	< 0.5	< 0.8	< 0.02	< 0.08	< 4.4	──
SXDS1_42087	0.73 ± 0.14	3.8 ± 0.7	7.6 ± 1.5	0.68 ± 0.15	0.19 ± 0.07	11 ± 4	722 ± 300
SXDS1_59863	0.74 ± 0.14	3.2 ± 0.6	4.8 ± 0.9	0.25 ± 0.04	< 0.18	< 9.9	> 480
SXDS1_59914	0.43 ± 0.12	1.9 ± 0.5	4.5 ± 1.3	0.39 ± 0.08	< 0.20	< 11	> 408
SXDS1_67002	< 0.17	< 0.6	< 1.3	< 0.27	0.09 ± 0.04	4.9 ± 2.2	< 261
SXDS1_68849	< 0.21	< 0.8	< 1.4	< 0.35	< 0.18	< 9.8	──
SXDS1_79307	< 0.11	< 0.6	< 2.0	< 0.09	< 0.12	< 6.7	──
SXDS1_79518	0.66 ± 0.17	2.4 ± 0.6	11 ± 3	0.81 ± 0.05	< 0.18	< 9.8	> 1079
SXDS2_13316	0.62 ± 0.21	2.7 ± 0.9	6.8 ± 2.3	0.89 ± 0.12	< 0.14	< 7.7	> 885
SXDS2_22198	< 0.10	< 0.5	< 0.7	< 0.30	0.10 ± 0.04	5.5 ± 2.2	< 124
SXDS3_101746	< 0.22	< 0.8	< 2.5	< 0.86	< 0.18	< 9.8	──
SXDS3_103139	< 0.12	< 0.5	< 2.4	< 0.61	< 0.08	< 4.4	──
SXDS3_110465	< 0.21	< 0.9	< 1.5	< 0.33	< 0.18	< 9.9	──
SXDS5_19723	0.38 ± 0.09	1.9 ± 0.4	4.1 ± 1.0	0.54 ± 0.14	< 0.08	< 4.4	> 921
SXDS5_28019	0.35 ± 0.06	1.3 ± 0.2	3.9 ± 0.7	0.57 ± 0.16	0.28 ± 0.08	15 ± 4	256 ± 86
SXDS5_9364	0.58 ± 0.17	2.5 ± 0.7	4.2 ± 1.2	0.48 ± 0.13	0.24 ± 0.10	13 ± 6	320 ± 162

[a]We adopted the CO(5-4)/CO(1-0) luminosity ratio of 0.23 (Daddi et al. 2015) and metallicity-dependent CO-to-H$_2$ conversion factor shown with the equation (3) (Genzel et al. 2012).

[b]$f_{gas} = \frac{M_{gas}}{M_{gas}+M_{star}}$

[c]The average observed wavelength is ~ 1.3 mm, thus, the average rest-frame wavelength is ~ 0.5 mm.

[d]We used a modified black body model adopting a dust temperature of 30 K and a dust emissivity index of 1.5.

Table 3

Results of the observations. (continued)

ID	noise level[e] (mJy/beam)	beam size, PA
SXDS1_13015	0.09	$0''.85 \times 0''.65$, $108°$
SXDS1_1723	0.10	$1''.28 \times 0''.64$, $72°$
SXDS1_31189	0.06	$0''.80 \times 0''.66$, $100°$
SXDS1_33244	0.07	$1''.04 \times 0''.64$, $75°$
SXDS1_35572	0.04	$0''.84 \times 0''.68$, $93°$
SXDS1_42087	0.06	$0''.80 \times 0''.66$, $96°$
SXDS1_59863	0.09	$0''.85 \times 0''.65$, $110°$
SXDS1_59914	0.10	$1''.20 \times 0''.65$, $73°$
SXDS1_67002	0.07	$0''.87 \times 0''.63$, $114°$
SXDS1_68849	0.09	$0''.96 \times 0''.65$, $76°$
SXDS1_79307	0.06	$0''.80 \times 0''.66$, $93°$
SXDS1_79518	0.09	$1''.02 \times 0''.65$, $75°$
SXDS2_13316	0.07	$0''.86 \times 0''.64$, $109°$
SXDS2_22198	0.04	$0''.86 \times 0''.68$, $86°$
SXDS3_101746	0.09	$1''.06 \times 0''.65$, $74°$
SXDS3_103139	0.04	$0''.83 \times 0''.68$, $100°$
SXDS3_110465	0.09	$1''.13 \times 0''.65$, $74°$
SXDS5_19723	0.04	$0''.83 \times 0''.68$, $97°$
SXDS5_28019	0.04	$0''.85 \times 0''.68$, $90°$
SXDS5_9364	0.08	$0''.87 \times 0''.64$, $112°$

[e]Noise level in continuum map.